

Mechanisms of hyperconcentrated flood propagation in a dynamic channel-floodplain system

Li, Wei; Su, Zhenghua; van Maren, Bas; Wang, Zhengbing ; de Vriend, Hubrecht

DOI

[10.1016/j.advwatres.2017.05.012](https://doi.org/10.1016/j.advwatres.2017.05.012)

Publication date

2017

Document Version

Accepted author manuscript

Published in

Advances in Water Resources

Citation (APA)

Li, W., Su, Z., van Maren, B., Wang, Z., & de Vriend, H. (2017). Mechanisms of hyperconcentrated flood propagation in a dynamic channel-floodplain system. *Advances in Water Resources*, 107, 470-489. <https://doi.org/10.1016/j.advwatres.2017.05.012>

Important note

To cite this publication, please use the final published version (if applicable). Please check the document version above.

Copyright

Other than for strictly personal use, it is not permitted to download, forward or distribute the text or part of it, without the consent of the author(s) and/or copyright holder(s), unless the work is under an open content license such as Creative Commons.

Takedown policy

Please contact us and provide details if you believe this document breaches copyrights. We will remove access to the work immediately and investigate your claim.

Mechanisms of hyperconcentrated flood propagation in a dynamic channel-floodplain system

Wei Li^{1,*}, Zhenghua Su¹, D. S. van Maren^{2,3}, Zhengbing Wang^{2,3}, Huib J. de Vriend^{2,3}

*Corresponding author. Tel: +8615957114735. E-mail addresses: lw05@zju.edu.cn.

¹Ocean College, Zhejiang University, Hangzhou/Zhoushan 310058, China

²Department of Hydraulic Engineering, Faculty of Civil Engineering and Geosciences, Delft University of Technology, P. O. Box 5048, 2600 GA Delft, The Netherlands

³Deltares, Rotterdamseweg 185, 2629 HD Delft, The Netherlands

Abstract

The downstream peak discharge increase during hyperconcentrated floods in the Yellow River has been attributed to bed erosion, roughness reduction and floodplain effects. While great improvements have been made on the understandings of the roles of bed erosion and roughness reduction, the effects of floodplain remain poorly understood. Here, as a first step to reveal the floodplain effects, we present a numerical experimental study on how the channel-floodplain system reacts to a hyperconcentrated flood process. For this purpose, schematized channel-floodplain systems are designed and the classical 1992 flood record data is prescribed at the upstream boundary. By applying a fully coupled morphodynamic model, numerical experiments are conducted for a comprehensive analysis on the effects of bed erodibility, floodplain width, bed roughness variation, symmetry and longitudinal variability of geomorphology. Our results show two distinct trends for the response of channel- floodplain system depending on bed erodibility. For a small bed erodibility, both channel and floodplain experience erosion. For a moderate/large bed erodibility, only the channel experiences erosion whereas deposition occurs on the floodplain. The variation of the floodplain width does not affect these erosion-deposition behaviors while changing the magnitude and patterns of floodplain deposition. The longitudinally discontinuous channel-floodplain divided by either water storage areas or housing/farming banks diminishes the floodplain deposition at the discontinuous locations. The present numerical experiments do not show an obvious peak discharge increase, nonetheless, the recognized erosion-deposition characteristics would help further study of the floodplain effects on the peak of hyperconcentrated floods.

Keywords: *Hyperconcentrated flood; floodplain effects; channel-floodplain system; coupled morphodynamic model; peak discharge; Yellow River.*

1 Introduction

Hyperconcentrated flow is a water-driven sediment transport phenomenon characterized by high sediment concentrations. It has been observed in a diversity of environmental settings. Many hyperconcentrated flows occur in volcanic terrains with recent eruptions by downstream diluting of debris flow (Pierson and Scott, 1985; Smith, 1986, 1987; Cronin et al., 2000; Lirer et al., 2001). Other initiation mechanisms include rainstorm-induced landslides and check-dam collapses in mountains (Pierson and Costa, 1987; Batalla et al., 1999; Sohn et al., 1999; Kostaschuk et al., 2003), breaking of debris-dammed lakes or reservoirs (Manville et al., 1999; Thouret, 1999; Capra, 2007; Wilcox et al., 2014), glacier-outburst floods (Maizels, 1989; Breien et al., 2008), collapses of aeolian damming and flash floods in desert ephemeral rivers (Laronne and Reid, 1993; Svendsen et al., 2003; Cohen and Laronne, 2005), submarine transition from debris flow (Sohn et al., 2002; Russell and Arnott, 2003), and flashing flood by reservoir turbidity currents (Hu et al., 2012).

In tributaries of the middle Yellow River (China) which spread on the highly erodible Loess Plateau, flow with sediment concentrations higher than 400 kg/m^3 is considered as hyperconcentrated flow (Xu, 1998). While in the main stream of the Yellow River this critical sediment concentration is considered to be 200 kg/m^3 (Zhang and Xie, 1993; Wan and Wang, 1994; Zhao, 1996; Xu, 2004). The hyperconcentrated flow in the Yellow River often occurs in the flood season and is usually treated as Newtonian, turbulent flow (Chien and Wan, 1983; Chien, 1989; Wang et al., 2002; van Maren et al., 2009a).

One interesting phenomenon associated with the hyperconcentrated flood (HF) is a downstream increasing peak discharge. In the period of 1970s-1990s, this phenomenon was observed seven times in the Xiaolangdi-Huayuankou reach (approximately 125.8 km) of the Lower Yellow River, for which the river channel was shallow and the floodplain was often inundated. The maximal increasing rate of the peak discharge was 30% from the Xiaolangdi to Huayuankou hydrological stations. After 2004 when the water-sediment regulation by the Xiaolangdi Reservoir became operational, hyperconcentrated floods were mostly conveyed inside the main channel and the average increasing rate was as high as 50%. Such increase in the peak discharge aggravates the flood risk at the downstream, and thus it is of great importance to unravel the underlying mechanisms. The main responsible mechanisms

have been attributed to the following issues. First, the later parts of the flood can be accelerated by bed roughness reduction related to high sediment concentration, and then catch up with the former flood possibly resulting in an increasing peak discharge at downstream (Jiang et al., 2006). Second, rapid and strong bed erosion during a HF may increase the water-sediment volume to a large extent probably causing an increasing peak discharge (Cao et al., 2006; Qi et al., 2010). Third, the rapid morphological change from a wide-shallow channel to a narrow-deep one through channel erosion and floodplain deposition may accelerate the flow velocity. A downstream increasing peak discharge may occur when the successive flood waves overlap the front flood peak (Wang et al., 2009). This effect may be strengthened by returning flow from floodplain to channel at the start of waning stage (Qi and Li, 1996).

Many investigations have been done for the first (Jiang et al., 2006; Li, 2008) and the second (Cao et al., 2006, 2012; Qi et al., 2010) mechanisms. For example, Li et al. (2014) compared the relative role of the first two mechanisms and discussed their coupling processes as well as their physical integration by the concept of channel storage. However, comprehensive in-depth analysis on the third mechanism is rare, except a few literal analyses based on limited field observations (Chien and Wan, 1983; Qi and Li, 1996; Wang et al., 2009). It is still unclear how bed deformation happens and to what extent it affects the flood propagation in the process of inundating floodplains.

In this regard, the first step should be a good understanding of how a channel-floodplain system reacts to a hyperconcentrated flood process. For this purpose, we conduct a process-based mechanism study on this issue using a 2-D depth-averaged fully coupled morphodynamic model. In our work, schematized channel-floodplain systems are designed and the classical 1992 flood record data is prescribed at the upstream boundary. A series of numerical experiments are done to answer the following questions: First, can the typical morphological features of channel erosion and floodplain deposition during a HF be successfully reproduced by the present 2-D depth-averaged model? And what is the relation between channel erosion and floodplain deposition? Second, how such morphological changes affect the flood propagation? Third, can a downstream increasing peak discharge be predicted when such morphological changes occur? Fourth, what are the impacts of initial reach profile in terms of the symmetric/asymmetric, longitudinally uniform/varying configurations?

2 Fully coupled morphodynamic model

2.1 Governing equations

Based on the concept of non-capacity sediment transport, the non-linear system of governing equations for the 2-D depth-averaged fully coupled morphodynamic model consists of the mass and momentum balance equations for sediment-laden flow, the mass balance equation for sediment, and a bed update equation. The vector form of the governing equations reads (Li et al., 2013)

$$\frac{\partial \mathbf{U}}{\partial t} + \frac{\partial \mathbf{F}}{\partial x} + \frac{\partial \mathbf{G}}{\partial y} = \mathbf{S}_0 + \mathbf{S}_f + \mathbf{S}_t \quad (1)$$

$$\mathbf{U} = \begin{bmatrix} h \\ hu \\ hv \\ hc \\ \phi \end{bmatrix}, \quad \mathbf{F} = \begin{bmatrix} hu \\ hu^2 + 0.5gh^2 \\ huv \\ huc \\ huc \end{bmatrix}, \quad \mathbf{G} = \begin{bmatrix} hv \\ hvu \\ hv^2 + 0.5gh^2 \\ hvc \\ hvc \end{bmatrix}, \quad (2a,b,c)$$

$$\mathbf{S}_0 = \begin{bmatrix} 0 \\ ghS_{0x} \\ ghS_{0y} \\ 0 \\ 0 \end{bmatrix}, \quad \mathbf{S}_f = \begin{bmatrix} \frac{E-D}{1-p} \\ -ghS_{fx} - \frac{(\rho_s - \rho_w)gh^2}{2\rho} \frac{\partial c}{\partial x} - \frac{(\rho_0 - \rho)(E-D)u}{\rho(1-p)} \\ -ghS_{fy} - \frac{(\rho_s - \rho_w)gh^2}{2\rho} \frac{\partial c}{\partial y} - \frac{(\rho_0 - \rho)(E-D)v}{\rho(1-p)} \\ E-D \\ 0 \end{bmatrix}, \quad (2d,e)$$

$$\mathbf{S}_t = \begin{bmatrix} 0 \\ \frac{\partial(h\tau_{xx})}{\partial x} + \frac{\partial(h\tau_{xy})}{\partial y} - \frac{(\rho_s - \rho_w)u}{\rho} \Phi_s \\ \frac{\partial(h\tau_{yx})}{\partial x} + \frac{\partial(h\tau_{yy})}{\partial y} - \frac{(\rho_s - \rho_w)v}{\rho} \Phi_s \\ \Phi_s \\ \Phi_s \end{bmatrix} \quad (2f)$$

where \mathbf{U} =vector of conservative variables; \mathbf{F}, \mathbf{G} =vectors of flux variables; \mathbf{S}_0 , \mathbf{S}_f , \mathbf{S}_t = vectors of source terms; $\phi = (1-p)z + hc$ = newly constructed conservative

variable; t = time; x = horizontal coordinate; y = horizontal coordinate; h = water depth; u = depth-averaged flow velocity in x direction; v = depth-averaged flow velocity in y direction; C = depth-averaged volumetric sediment concentration; z = bed elevation; $\rho = \rho_w(1-c) + \rho_s c$ = density of sediment-laden flow; $\rho_s = 2650$ kg/m³ is sediment density; $\rho_w = 1000$ kg/m³ is water density; $\rho_0 = \rho_w p + \rho_s(1-p)$ = density of saturated bed; p = bed porosity; g = acceleration of gravity; E, D = sediment entrainment and deposition fluxes respectively; S_{0x} = bed slope in x direction, expressed as $S_{0x} = -\partial z / \partial x$; S_{0y} = bed slope in y direction, expressed as $S_{0y} = -\partial z / \partial y$; S_{fx} = friction slope in x direction; S_{fy} = friction slope in y direction; $\tau_{xx}, \tau_{yy}, \tau_{xy}, \tau_{yx}$ = depth-averaged Reynolds stresses, expressed as $\tau_{xx} = 2v_t \partial u / \partial x, \tau_{yy} = 2v_t \partial v / \partial y, \tau_{xy} = \tau_{yx} = v_t(\partial u / \partial y + \partial v / \partial x)$; v_t = turbulent eddy viscosity; $\Phi_s = \partial(h\varepsilon_s \partial c / \partial x) / \partial x + \partial(h\varepsilon_s \partial c / \partial y) / \partial y$ = sediment dispersion/diffusion terms; ε_s = sediment dispersion/diffusion coefficient.

2.2 Numerical scheme

The present model is an advanced version of a previous one which is second order accurate in space and time (Li et al., 2013). The main improvement is the satisfactory of the well-balanced property (i.e., retaining the initial static flow over irregular beds). This is achieved by applying the surface gradient method (SGM) (Zhou et al., 2001) to the original UFORCE scheme (Stecca et al., 2010) in terms of flux computation. As we use a standard splitting approach (Toro, 2001) in time integration of the governing equations, the effect of bed slope is considered in solving the homogeneous part when the SGM version is adopted. Here, we only elaborate the SGM-version of the UFORCE scheme in flux computation and the corresponding modification of the time integration method. For other details of the numerical scheme such as wetting-drying procedure and the treatment of spatial gradient of concentration in source terms, one can refer to our previous work (Li et al., 2013; Li et al., 2014).

2.2.1 Method of time integration

The governing equations are discretized using a collocated cell-centered FVM, with which the average values of conserved variables being defined at the centre (Li et al., 2013). For the time integration of the discretized equations, a standard splitting approach is deployed together with a second order Runge-Kutta method (Toro, 2001, 2009). The SGM-version differs from the original model of depth gradient method

(DGM) when moving the bed slope term from the source term of the second splitting step (Li et al., 2013) to the homogeneous equation of the first splitting step, which reads

$$\mathbf{U}_{i,j}^* = \mathbf{U}_{i,j}^n - \frac{\Delta t}{\Delta x} (\mathbf{F}_{i+1/2,j} - \mathbf{F}_{i-1/2,j}) - \frac{\Delta t}{\Delta y} (\mathbf{G}_{i,j+1/2} - \mathbf{G}_{i,j-1/2}) + \Delta t \mathbf{S}_{0i,j}^* \quad (3a)$$

$$\mathbf{U}_{i,j}^{n+1} = \mathbf{U}_{i,j}^* + 0.5 \times (\mathbf{K}_1 + \mathbf{K}_2) \quad (3b)$$

with

$$\mathbf{S}_{0i,j}^* = \begin{bmatrix} 0 \\ -g \frac{h_{i+1/2,j}^{L*} + h_{i-1/2,j}^{R*}}{2} \frac{z_{i+1/2,j} - z_{i-1/2,j}}{\Delta x} \\ -g \frac{h_{i,j+1/2}^{L*} + h_{i,j-1/2}^{R*}}{2} \frac{z_{i,j+1/2} - z_{i,j-1/2}}{\Delta y} \\ 0 \\ 0 \end{bmatrix} \quad (4)$$

$$\mathbf{K}_1 = \Delta t (\mathbf{S}_f(\mathbf{U}_{i,j}^*) + \mathbf{S}_t(\mathbf{U}_{i,j}^*)), \quad \mathbf{K}_2 = \Delta t (\mathbf{S}_f(\mathbf{U}_{i,j}^* + \mathbf{K}_1) + \mathbf{S}_t(\mathbf{U}_{i,j}^* + \mathbf{K}_1)) \quad (5a,b)$$

where $\Delta x, \Delta y$ = spatial steps in x - and y - directions; i, j = cell indices in x and y directions; $\mathbf{U}_{i,j}$ = vector of cell-averaged conservative variable at the center; $\mathbf{F}_{i+1/2,j}$, $\mathbf{F}_{i-1/2,j}$, $\mathbf{G}_{i,j+1/2}$, $\mathbf{G}_{i,j-1/2}$ = vectors of normal flux at interfaces $(i+1/2, j)$, $(i-1/2, j)$, $(i, j+1/2)$, $(i, j-1/2)$; $\mathbf{U}_{i,j}^*$ = vector of predictor variables at the intermediate stage; $\mathbf{U}_{i,j}^n, \mathbf{U}_{i,j}^{n+1}$ = vectors of conservative variables at the time step $n, n+1$; $\mathbf{S}_{0i,j}^*$ = vector of bed slope-related term in SGM version; $h_{i+1/2,j}^{L*}, h_{i,j+1/2}^{L*}, h_{i-1/2,j}^{R*}, h_{i,j-1/2}^{R*}$ = extrapolated water depth at the left and right sides of cell interface at the intermediate stage; $z_{i+1/2,j}, z_{i-1/2,j}, z_{i,j+1/2}, z_{i,j-1/2}$ = bed elevation at cell interface; Δt = computational time step. The spatial gradients of bed level and source-term sediment concentration are discretized by centered difference scheme.

2.2.2 Method of flux computation

The SGM version of the UFORCE scheme has three steps for computing the advection flux in x - direction. In y - direction, the method is analogous. As the

third step is the same as our previous model (Li et al., 2013), here we only elaborate the first two steps for concise.

Step 1: MUSCL reconstruction

In order to achieve second order accuracy in space, the cell interface values are extrapolated from the cell center values by a limited slope. Based on the SGM (Zhou et al., 2001), the water depth is obtained by free surface reconstruction as

$$\zeta_{i+1/2,j}^L = \zeta_{i,j}^n + 0.5\overline{\Delta}_i^\zeta, \quad \zeta_{i+1/2,j}^R = \zeta_{i+1,j}^n - 0.5\overline{\Delta}_{i+1}^\zeta \quad (6a,b)$$

$$h_{i+1/2,j}^L = \zeta_{i+1/2,j}^L - z_{i+1/2,j}, \quad h_{i+1/2,j}^R = \zeta_{i+1/2,j}^R - z_{i+1/2,j} \quad (7a,b)$$

with

$$\overline{\Delta}_i^\zeta = \begin{cases} \zeta_{i+1,j}^n - \zeta_{i,j}^n & \text{if } |\zeta_{i+1,j}^n - \zeta_{i,j}^n| \leq |\zeta_{i,j}^n - \zeta_{i-1,j}^n| \\ \zeta_{i,j}^n - \zeta_{i-1,j}^n & \text{else} \end{cases} \quad (8)$$

$$z_{i+1/2,j} = (z_{i,j} + z_{i,j+1}) / 2 \quad (9)$$

where ζ = water level; $\overline{\Delta}^\zeta$ = limited slope for water level.

Other conservative variables are reconstructed following Stecca et al. (2010)

$$\mathbf{U}_{i+1/2,j}^L = \mathbf{U}_{i,j}^n + 0.5\overline{\Delta}_i, \quad \mathbf{U}_{i+1/2,j}^R = \mathbf{U}_{i+1,j}^n - 0.5\overline{\Delta}_{i+1} \quad (10a, b)$$

With

$$\overline{\Delta}_i = \begin{cases} \mathbf{U}_{i+1,j}^n - \mathbf{U}_{i,j}^n & \text{if } |\mathbf{U}_{i+1,j}^n - \mathbf{U}_{i,j}^n| \leq |\mathbf{U}_{i,j}^n - \mathbf{U}_{i-1,j}^n| \\ \mathbf{U}_{i,j}^n - \mathbf{U}_{i-1,j}^n & \text{otherwise} \end{cases} \quad (11)$$

where $\mathbf{U}_{i+1/2,j}^L$, $\mathbf{U}_{i+1/2,j}^R$ = vectors of extrapolated variables at the left and right sides

of the interface between cells (i, j) and $(i+1, j)$; $\overline{\Delta}_i$, $\overline{\Delta}_{i+1}$ = vectors of limited slope.

Here the limited slope is computed by the ENO (Essentially Non Oscillatory) approach (Harten et al., 1987) to avoid spurious oscillations near large gradients (Stecca et al., 2010).

Step 2: State evolution by $\Delta t / 2$

The cell interface variables are further evolved over a half time step to reach second order accuracy in time. In this step, the SGM version of the UFORCE scheme considers the bed slop-related term for state evolution:

$$\begin{aligned} \mathbf{U}_{i+1/2,j}^{L*} = & \mathbf{U}_{i+1/2,j}^L + \frac{\Delta t}{2\Delta x} \left[\mathbf{F}(\mathbf{U}_{i-1/2,j}^R) - \mathbf{F}(\mathbf{U}_{i+1/2,j}^L) \right] \\ & + \frac{\Delta t}{2\Delta y} \left[\mathbf{G}(\mathbf{U}_{i,j-1/2}^R) - \mathbf{G}(\mathbf{U}_{i,j+1/2}^L) \right] + \frac{\Delta t}{2} \mathbf{S}_{0i,j} \end{aligned} \quad (12a)$$

$$\begin{aligned} \mathbf{U}_{i+1/2,j}^{R*} = & \mathbf{U}_{i+1/2,j}^R + \frac{\Delta t}{2\Delta x} \left[\mathbf{F}(\mathbf{U}_{i+1/2,j}^R) - \mathbf{F}(\mathbf{U}_{i+3/2,j}^L) \right] \\ & + \frac{\Delta t}{2\Delta y} \left[\mathbf{G}(\mathbf{U}_{i+1,j-1/2}^R) - \mathbf{G}(\mathbf{U}_{i+1,j+1/2}^L) \right] + \frac{\Delta t}{2} \mathbf{S}_{0i+1,j} \end{aligned} \quad (12b)$$

with

$$\mathbf{S}_{0i,j} = \begin{bmatrix} 0 \\ -g \frac{h_{i+1/2,j}^L + h_{i-1/2,j}^R}{2} \frac{z_{i+1/2,j} - z_{i-1/2,j}}{\Delta x} \\ -g \frac{h_{i,j+1/2}^L + h_{i,j-1/2}^R}{2} \frac{z_{i,j+1/2} - z_{i,j-1/2}}{\Delta y} \\ 0 \\ 0 \end{bmatrix} \quad (13)$$

For the UFORCE flux computation, one can refer to Li et al. (2013) for detail.

2.3 Empirical relations and parameters

The friction slope is estimated by Manning roughness coefficient n , as

$$S_{fx} = n^2 u \sqrt{u^2 + v^2} / h^{4/3}, \quad S_{fy} = n^2 v \sqrt{u^2 + v^2} / h^{4/3} \quad (14a,b)$$

It should be noted that the Manning roughness coefficient is calculated by two methods. For most of the simulated cases focusing on the influences of channel-floodplain system, we assume that bed roughness is invariant and a constant Manning roughness coefficient is set. Only in the cases for investigating the effects of roughness change, we use an empirical formulation (Zhao and Zhang, 1997) to incorporate both hydraulic and sedimentary effects on Manning roughness (Li et al., 2014),

$$n = \frac{h^{1/6}}{\sqrt{g}} c_n \frac{\delta_*}{h} \left\{ 0.49 \left(\frac{\delta_*}{h} \right)^{0.77} + \frac{3\pi}{8} \left(1 - \frac{\delta_*}{h} \right) \left[\sin \left(\frac{\delta_*}{h} \right)^{0.2} \right]^5 \right\}^{-1} \quad (15)$$

with

$$c_n = 0.375\kappa \quad (16)$$

$$\kappa = 0.4 - 1.68(0.365 - c)\sqrt{c} \quad (17)$$

$$\delta_* = D_{50} \left(1 + 10^{8.1 - 13Fr^{0.5}(1 - Fr^3)} \right) \quad (18)$$

where δ_* = friction thickness; Fr = Froude number; D_{50} = median diameter of bed material (m); c_n = vortex coefficient; κ = Von Karman coefficient in turbid flow; C = depth-averaged volumetric sediment concentration.

For numerical experiments of the 1992 HF in a channel-floodplain system, the sediment entrainment and deposition fluxes are estimated using the Partheniades-Krone formulations (Partheniades, 1965). This formula is valid for very fine sediments, and has been satisfactorily applied to a detailed 3-D modeling of a Yellow River HF in a channel-floodplain reach by the Delft3D software (van Maren et al., 2009b). The formulations are:

$$E = \begin{cases} \frac{M}{\rho_s} (\tau / \tau_{cr,e} - 1) & \text{for } \tau > \tau_{cr,e} \\ 0 & \text{for } \tau < \tau_{cr,e} \end{cases} \quad (19a,b)$$

$$D = \begin{cases} \omega_s c (1 - \tau / \tau_{cr,d}) & \text{for } \tau < \tau_{cr,d} \\ 0 & \text{for } \tau > \tau_{cr,d} \end{cases} \quad (20a,b)$$

where M = erosion rate ($\text{kg/m}^2/\text{s}$); ω_s = effective sediment settling velocity (m/s); τ = bed shear stress (Pa); $\tau_{cr,e}, \tau_{cr,d}$ = critical bed shear stresses for erosion and deposition, respectively (Pa). Other parameters are the same as those specified above. In the numerical experiments, the value of $M, \tau_{cr,e}, \tau_{cr,d}$ is specified case by case. The effective sediment settling velocity ω_s is calculated by considering hindered settling effect in hyperconcentration (Richardson and Zaki, 1954),

$$\omega_s = \omega_0 \left(1 - \frac{c}{1-p}\right)^5 \quad (21)$$

With ω_0 calculated by Zhang and Xie (1993)'s formula:

$$\omega_0 = \sqrt{(13.95\nu/d)^2 + 1.09(\rho_s - \rho_w)gd/\rho_w} - 13.95\nu/d \quad (22)$$

where d = sediment diameter (m); ω_0 = settling velocity of a single particle in clear and still water (m/s); $\nu = 10^{-6}$ is kinematic viscosity of water. Other parameters are the same as those specified above.

Since the majority of the sediment transported in the Middle and Lower Yellow River is composed of suspended load (Long and Zhang, 2002), we only consider suspended load in the present numerical experiments. In overbank flows turbulent eddy viscosity and diffusion coefficient for suspended load are estimated following the method by Li et al. (2013). Both the horizontal and vertical production of turbulence (Jia and Wang, 1999; Cea et al., 2007) are considered in the estimation of turbulent eddy viscosity using a mixing length model. The roles of different turbulence closure models on the erosion/deposition processes are analyzed later in the discussion section.

2.4 Numerical stability and model test

As for the numerical stability, the CFL condition is deployed to restrict the computational time step in all the model runs. Note that the usual stability limitation for the upwind-biased FORCE type schemes should be $0 < \text{CFL} < 0.5$ in the two-dimensional Cartesian meshes (Siviglia et al., 2013; Stecca et al., 2012; Stecca et al., 2010). We therefore use $\text{CFL} = 0.45$ for all the cases in the present paper.

With model application to the HF modelling in a channel-floodplain system, two issues should be addressed. On one hand, the HF are often highly unsteady together with high sediment concentration and rapid/strong morphological changes. It requires the model to accurately capture those features without oscillations. On the other hand, the overflowing on the previously dry floodplains and the possible flood detention by strong floodplain deposition challenge the model capability to well capture the moving dry-wet fronts and reserve the static state in complex topography. Therefore, before application to the HF modelling, these model abilities are tested and shown in Appendix.

3 Field observations

During a HF that occurred in August 1992 (Fig. 1), the measured flood peaks at the Xiaolangdi hydrological station were 3560, 3050, 3600, 4550 m³/s respectively. At the Huayuankou hydrological station (125.8 km downstream of Xiaolangdi), the second to the fourth flood peaks were observed to increase to 3230, 4080, 6430 m³/s respectively. The maximal sediment concentrations (in volume) corresponding to the four successive flood peaks at Xiaolangdi were 0.0777 (206 kg/m³), 0.078 (207 kg/m³), 0.163 (432 kg/m³), 0.198 (525 kg/m³) respectively, which were slightly higher than those at Huayuankou. In the Xiaolangdi-Huayuankou reach, overflowing on floodplains occurred when this flood passed by.

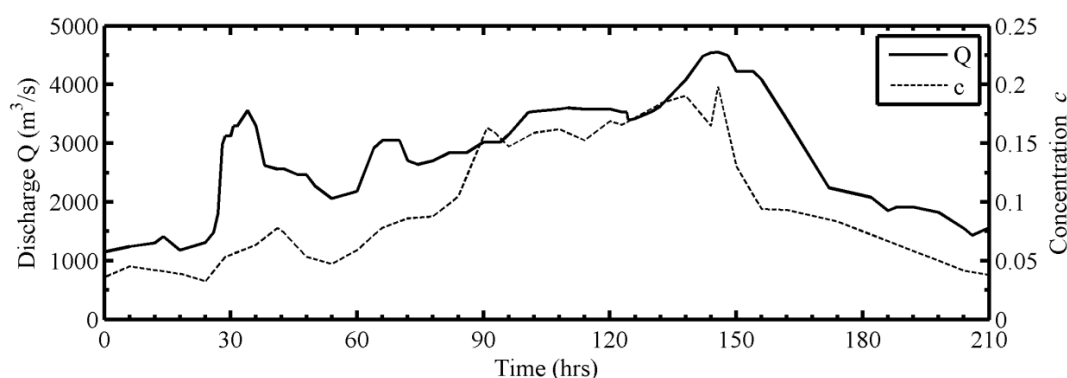


Figure 1 Measured discharge hydrograph and sediment concentration in the 1992 HF at Xiaolangdi.

Due to the logistic difficulties in measuring topography under HF conditions, bathymetric data for this flood is not available. As an alternative, we use two distinct cross-sectional profiles (before the flood season) at Huayuankou in 1993 and 1994 respectively to represent main features of channel-floodplain topography in this reach. One is an asymmetric channel-floodplain reach (Fig. 2a). For this type, one side of the reach is sufficiently high to prevent overflowing, while flood may inundate floodplain on the other low side. The other is a symmetric channel-floodplain reach (Fig. 2b), of which both sides are almost equally high. Therefore, floodplains on both sides may be simultaneously inundated when overflowing occurs.

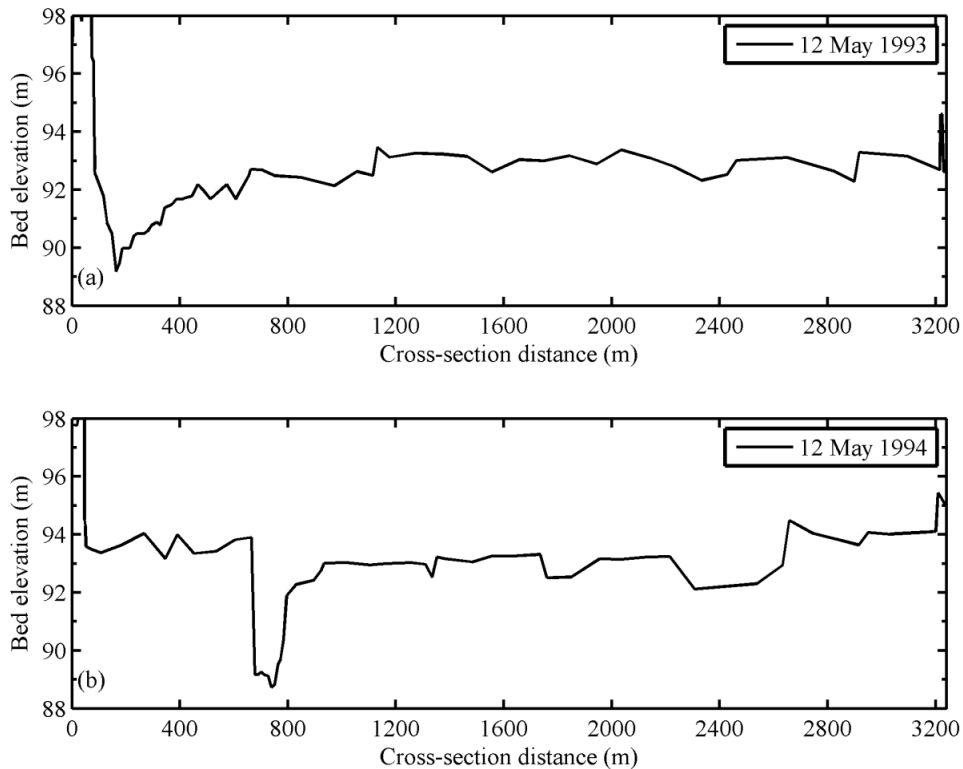


Figure 2 Measured cross-sectional profiles at Huayuankou in (a) 1993, (b) 1994.

4 Modeling of the 1992 HF

4.1 Topography schematization

Due to lack of sufficient data (both hydrographic and topographic) it is difficult to develop a predictive model that is well calibrated and validated by observations in the Yellow River. However, numerical experiments in a schematized channel-floodplain reach can offer an alternative solution for the process-based mechanism study. Here, the schematized reach consists of two sub-reaches: an upper narrow channel reach and a lower channel-floodplain reach (see Fig. 3). Concerning the main features of the cross-sectional profile in the Yellow River (Fig. 2), both asymmetric and symmetric configurations are considered in the lower channel-floodplain reach for comparison.

The upper narrow channel reach is designed to be sufficiently long and composed of rectangular cross-sections of constant width, because: (1) it provides sufficient distance for flow adaptation so that a stable flow condition can be obtained at the start of the channel-floodplain reach; (2) it avoids uncertainties arising from giving empirical relations for the lateral distribution of flow discharge and sediment concentration if floodplain is present at the upstream boundary.

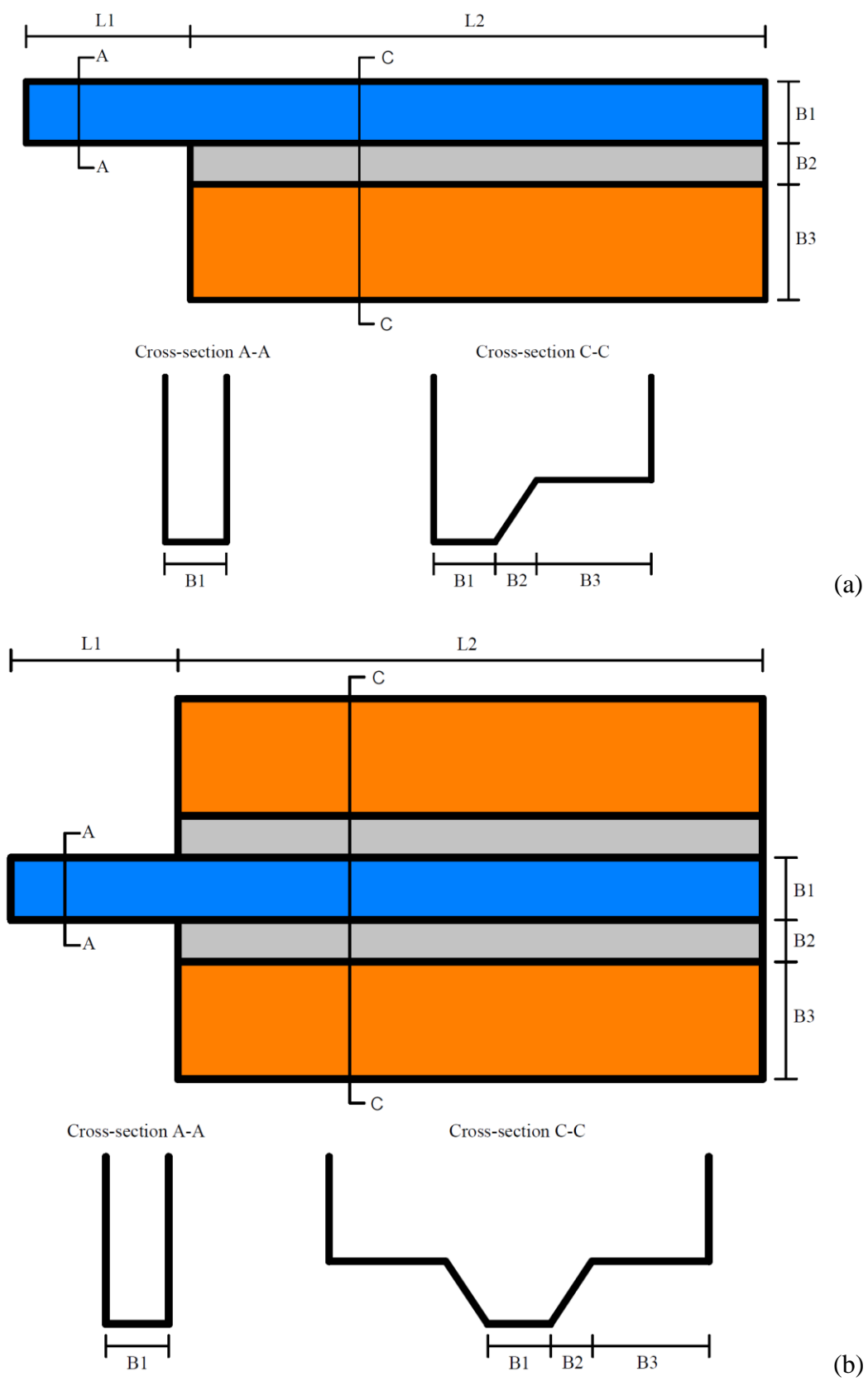


Figure 3 Schematized channel-floodplain reach (a) asymmetric, (b) symmetric.

4.2 Model setup

Eight cases are designed for experiments (see Tab. 1). In these cases, the initial flow conditions are obtained by first running the model over a fixed bed with a constant small discharge (under which no overflows occur) until it reaches a steady state (which takes some 60 hr in the present simulations). In model runs, the two tolerance depths for judging the dry and partially dry cells are set to 0.01 m and 0.05 m, respectively.

The schematic reach is composed of an upper narrow channel of 20 km long and a lower channel-floodplain reach of 140 km. Based on limited topographic data at the Xiaolangdi and Huayuankou hydrological stations in 1993, a bed slope of 3.0×10^{-4} is used for both the channel and the floodplain. In the upper narrow channel, a width of 300 m (see B_1 in Fig. 3) is set approximating the channel width at Xiaolangdi. In the lower channel-floodplain reach, the bottom channel width remains the same as that in the upper narrow channel and a total cross-sectional width of 1100 m is considered by averaging total widths at Xiaolangdi and Huayuankou (Cases 1-3, 6-8). The main channel is 1.6 m deep with a top channel width of 500 m. Accordingly, the symmetric type has a width of 100 m for a single channel side slope (B_2 in Fig. 3) and a width of 300 m for a single floodplain (B_3 in Fig. 3). The corresponding values for the asymmetric type are 200 m and 600 m (Cases 1-3 and 8) respectively. Different floodplain width, i.e., $B_3=400$ m for Case 4 and 300 m for Case 5, are also simulated in the asymmetric type for comparison.

In relation to sediment transport, uniform sediment is considered: $d_{50}=0.025$ mm, $p=0.45$. In most cases, the critical bed shear stresses for erosion ($\tau_{cr,e}$) and deposition ($\tau_{cr,d}$) are set at 1.0 and 0.9 Pa, respectively, which are close to the values used by van Maren et al. (2009b) for the 1959 HF of the Lower Yellow River with a Delft3D model. Additionally, large ($\tau_{cr,e}=1.6$ Pa, $\tau_{cr,d}=1.5$ Pa in Case 7) values are also used for comparison. In an attempt to reproduce the typical morphological feature of channel erosion and floodplain deposition during HF, different bed erodibility is considered by testing the parameter of erosion rate M . The range of the M value is chosen in reference to van Maren et al. (2009b). The results of $M=1.0 \times 10^{-4}$ (Case 2), 2.5×10^{-4} (Case 1), 5.0×10^{-4} (Case 3) are shown for the analysis. As bed roughness change (Li et al., 2014) is not the focus of the present work, we use a

constant Manning roughness of 0.011 (typical value for the LYR) in most cases. Only Case 8 considers a varied roughness for comparison.

Table 1 Numerical cases and model settings

Case	Reach type ^a	Channel and floodplain width (m)			Erosion and deposition parameters			Manning roughness
		B1	B2	B3	M	$\tau_{cr,e}$	$\tau_{cr,d}$	
1	A	300	200	600	2.5×10^{-4}	1.0	0.9	0.011
2	A	300	200	600	1.0×10^{-4}	1.0	0.9	0.011
3	A	300	200	600	5.0×10^{-4}	1.0	0.9	0.011
4	A	300	200	400	2.5×10^{-4}	1.0	0.9	0.011
5	A	300	200	300	2.5×10^{-4}	1.0	0.9	0.011
6	S	300	100	300	1.0×10^{-4}	1.0	0.9	0.011
7	S	300	100	300	2.5×10^{-4}	1.6	1.5	0.011
8	A	300	200	600	1.0×10^{-4}	1.0	0.9	Eq. (15)

^aIn the reach type, the abbreviation A means asymmetric, S means symmetric.

5 Results of the 1992 HF in the asymmetric channel-floodplain

5.1 Typical morphological features and their relations

With a suitable erosion rate (M), the typical morphological features of channel erosion and floodplain deposition during HF can be successfully reproduced by the present 2-D depth-averaged model. As an illustration, the time variations of cross-sectional profiles at x=40 km are shown in Fig. 4 for Cases 1-3 with different erosion rates.

With a moderate erosion rate of $M=2.5 \times 10^{-4}$ kg/m²/s in Case 1, continuous erosion (-0.5~-0.7 m) occurs in both the channel and the transitional area of channel-floodplain while sedimentation is observed in the middle area of the floodplain (Fig. 4a). The sediment deposition is strongest during the second flood period (t=60-90 hr), amounting to a deposit height up to 0.2 m. This is possibly because that the sediment concentration increases to a large extent specially after the second flood peak while the relatively small increase of flow discharge is insufficient to maintain the transport of so much sediment (see Fig. 1). During the third and fourth flood peaks (t=90-150 hr), the deposits are slightly eroded, probably due to an increase in bed shear stress with relatively large discharge. In the waning stage (after

150 hr), the deposit height increases again following the decrease of flow discharge and sediment concentration.

With a smaller erosion rate of $M=1.0 \times 10^{-4}$ kg/m²/s in Case 2, the channel erosion becomes much weaker and floodplain deposition only occurs in the waning stage after 150 hr (Fig. 4b). The less channel deepening in Case 2 results in a higher flow velocity and larger water depth on the floodplain, which corresponds with a relatively high bed shear stress. This yields no deposition or even minor erosion on the floodplain during the flood peak periods. Moreover, the suspended load becomes less in the case of weaker channel erosion (see Fig. 5 for the sediment concentration distribution just before the occurrence of floodplain deposition), which also contributes to less floodplain sedimentation.

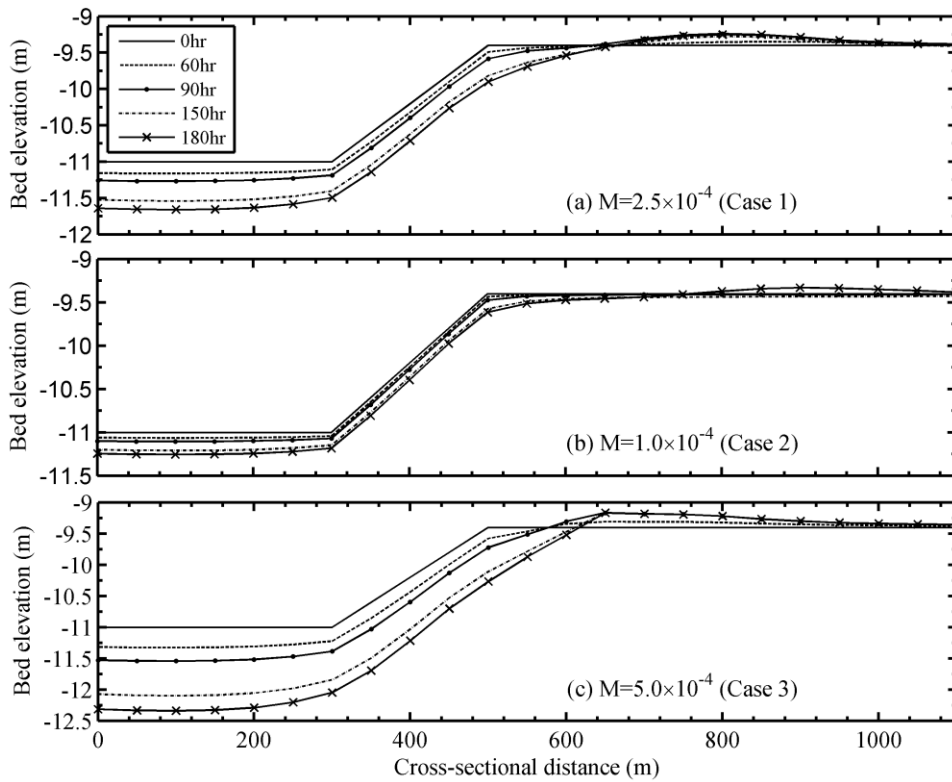


Figure 4 Cross-sectional morphological changes at $x=40$ km for (a) Case 1 with $M=2.5 \times 10^{-4}$, (b) Case 2 with $M=1.0 \times 10^{-4}$, (c) Case 3 with $M=5.0 \times 10^{-4}$.

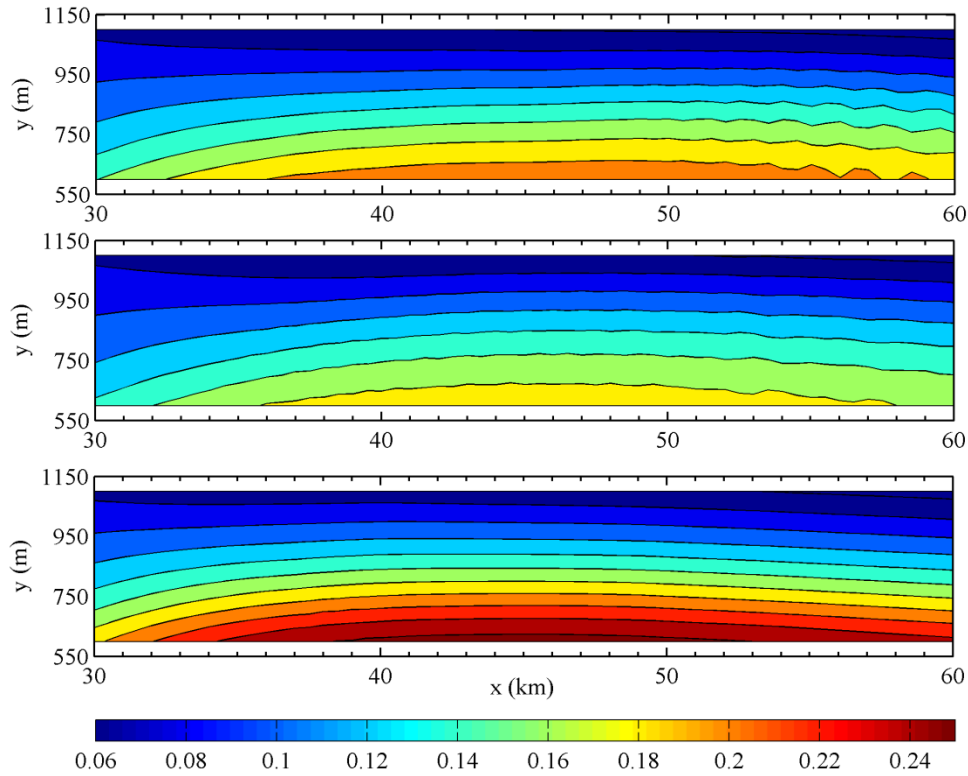


Figure 5 Contours of volumetric sediment concentration (unit: -) at $t=60$ hr in the floodplain area near $x=40$ km, for Case 1 (upper), Case 2 (middle), and Case 3 (lower).

With a larger erosion rate of $M=5.0 \times 10^{-4}$ kg/m²/s in Case 3, the floodplain deposition is strengthened with stronger channel erosion (Fig. 4c). The deposits move more closely towards the channel with a maximal height of about 0.25 m at $t=90$ hr. The stronger channel erosion causes shallow flows of small velocity together with more sediment available for deposition on the floodplain (see Fig. 5). As a result, relatively large sedimentation occurs on the floodplain due to a small bed shear stress and high sediment concentration. After the second flood (i.e., $t>90$ hr) there is hardly morphological change on the floodplain though the channel and the transitional area are continuously eroded. This indicates that the channel deepening and the height of previous floodplain deposition may be so large that not enough overflows can occur even if the fourth flood peak is much higher than the first two. Therefore, some parts of the floodplain might become almost dry and no deformation is observed.

5.2 Flood propagation

The numerical results show that the behavior of channel erosion and floodplain deposition can play an important role in the downstream HF propagation (see Fig. 6). In Cases 1 and 2, the channel erosion is not so considerable that the shallow flow on the floodplain is sufficiently deep to transport large portion of suspended sediment without the occurrence of dry areas. Therefore, the peak discharge is observed to decrease uniformly in the downstream direction by friction effects in these two cases. Their most distinguishable difference is the evolution of the second flood peak in the periods of 60-90 hrs. For Case 1 the peak discharge decreases slightly in the downstream (Fig. 6a), when the channel erosion and floodplain deposition are in a moderate range (Fig. 4a). However, the second flood peak of Case 2 follows a more obvious decreasing trend (Fig. 6b) when only minor channel erosion occurs with almost no floodplain deformation (Fig. 4b).

In comparison with Cases 1 and 2, Case 3 exhibits considerably different behavior from the second to the fourth flood processes. In the period of 60-90 hrs, relatively large channel erosion and floodplain deposition are observed in Case 3 (Fig. 4c). Such cross-sectional changes may play an important role in offsetting the effect of bed friction on flood peak attenuation. Therefore, an almost constant peak discharge of the second flood peak is predicted in the downstream direction (Fig. 6c). For the third and fourth flood peaks of Case 3, the peak discharge does not decrease as uniformly as it does in Cases 1 and 2. There is a considerable decrease of peak discharge at $x=40$ km while relatively small and uniform decrease of peak discharge is observed in further downstream. The considerable discharge decrease is probably because that the previous floodplain deposition is so high that the upstream flow may be blocked or decelerated in some areas of the floodplain. Moreover, the strong channel deepening during the third and fourth floods (Fig. 4c) may weaken the flood overtopping and thus shallow flow with small velocity or even still water area may occur on the floodplain contributing to a decrease of discharge peak. In further downstream ($x>40$ km), the magnitude of floodplain deposition and channel erosion may decrease with distance through the adaptation of the sediment transport capacity and suspended load. Therefore, their effect on the discharge evolution may be weakened or diminish with distance, and a uniform decrease of peak discharge is again observed in the downstream direction.

Regarding the satisfactory reproducing of typical morphological change and smooth prediction of flood processes, the moderate erosion rate of $M=2.5 \times 10^{-4}$ kg/m²/s is used for further numerical analysis of the influence of floodplain width.

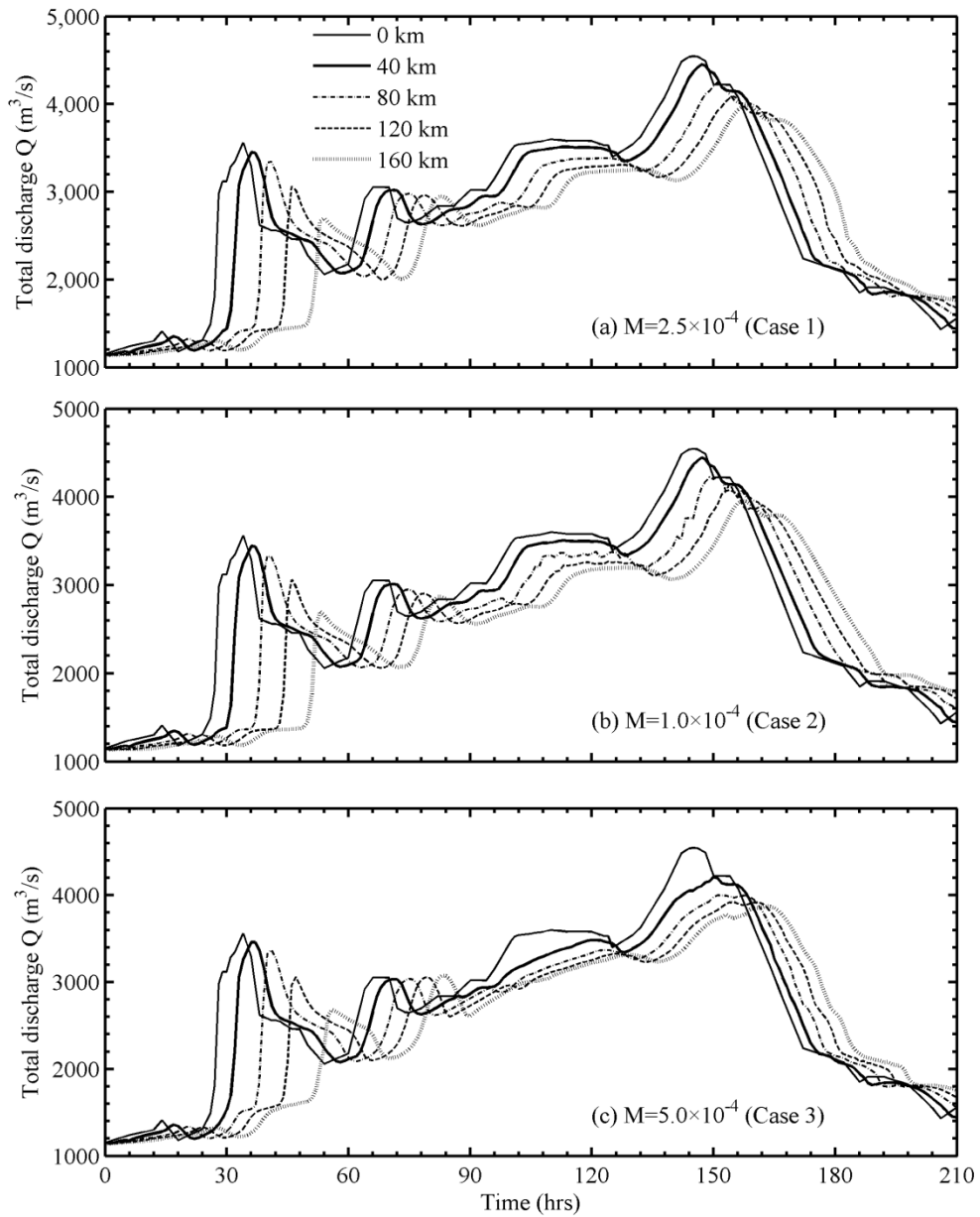


Figure 6 Computed discharge evolution for (a) Case 1 with $M=2.5 \times 10^{-4}$, (b) Case 2 with $M=1.0 \times 10^{-4}$, (c) Case 3 with $M=5.0 \times 10^{-4}$.

5.3 Influences of different floodplain width

Considering the interactions between channel erosion and floodplain deposition, we further investigate how the floodplain width influences the morphological behaviors and the discharge propagation. Compared with the floodplain width of $B_3=600$ m in Case 1, narrower values of $B_3=400$ m (Case 4) and $B_3=300$ m (Case 5) are used for modelling while other parameters are specified the same.

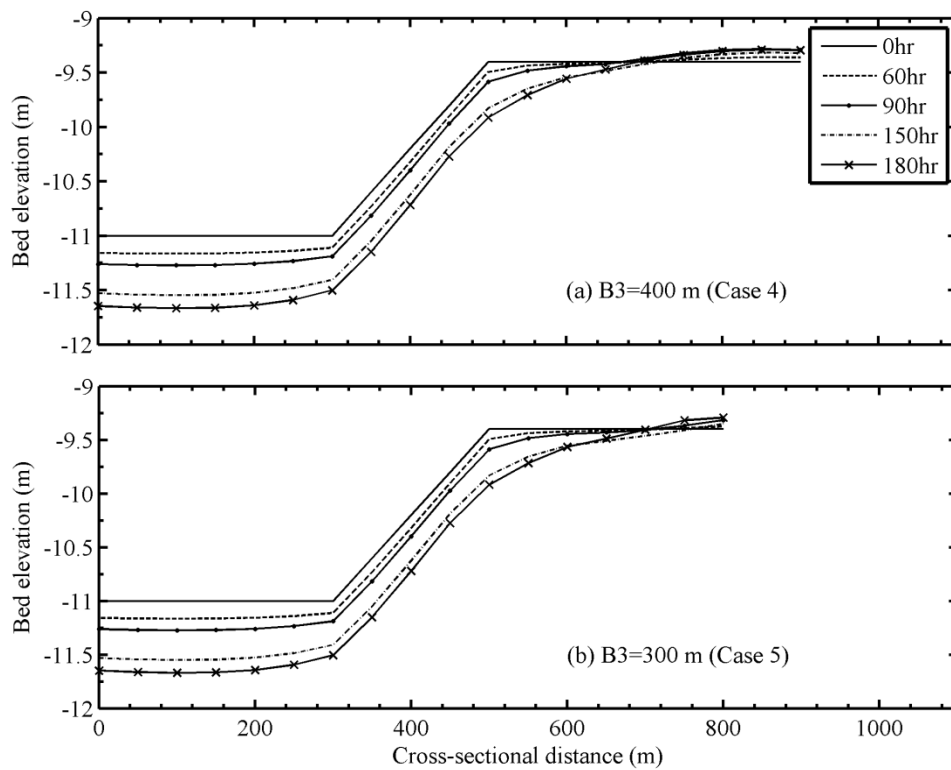


Figure 7 Cross-sectional changes for (a) Case 4 with $B_3=400$ m, and (b) Case 5 with $B_3=300$ m.

The results show that the floodplain width marginally affect channel erosion patterns whereas it plays a significant role in shaping floodplain deposition. In Cases 1, 4 and 5, the channel erosion processes are nearly the same (see Figs. 4a, 7) when identical model parameters for erosion and sedimentation are used. Only with decreasing floodplain width, the transitional point of erosion and deposition on the floodplain move closer to the sidewall (right). However, the patterns of floodplain deposition exhibit different features for different floodplain width. For a sufficiently wide floodplain in Case 1, the sediment deposition profile can be fully developed. The

highest deposition occurs in the middle of the floodplain (around $y=800$ m along the cross-section) when gradually weakened deposition appears in the lateral directions. For a narrow floodplain in Cases 4 and 5, the overtopping flow and associated sediment transport may be strongly restrained by the limited floodplain width, thus the deposition cannot be sufficiently developed (see Fig. 7). The strongest deposition is observed near the sidewall (right) of a narrow floodplain where the flow velocity tends to be small, and the magnitude of deposition is much smaller than that on a wide floodplain (comparing Fig. 4a and Fig. 7).

For the discharge propagation, the floodplain width has a strong impact on the first discharge peak especially in the downstream reach while the later discharge peaks are not affected so much along the course. In the upstream part ($x=40$ km), the effects of floodplain width on flow movement is not so obvious that the hydrographs are almost the same for different cases (Fig. 8a). However, the cumulative effects of floodplain width increase with distance, and the difference of hydrographs therefore becomes visible (Fig. 8b, 9). In the downstream reach ($x \geq 80$ km), the wider the floodplain is, the smaller and slower are the magnitude and the propagation of the first peak discharge respectively. This is probably due to more energy loss by bed friction in wider areas. On a wider floodplain, the overtopping flow can expand to a larger area causing smaller water depth. This results in a stronger friction effect and thus the discharge peak is more dampened. Along the course, the discrepancy of the first flood peak for Cases 1,4,5 increases due to cumulative effects. For the later discharge peaks, the hydrographs for different cases have very similar patterns. This is possibly because after the first flood, the floodplains are fully inundated with sufficient water depth. The successive floods further increase the inundation depth mitigating the effects of different energy loss related to bed friction. Moreover, the floodplain deposition is much weaker when compared with the channel erosion for these cases (Figs. 4a, 7), so the discharge propagation should mainly depend on the channel erosion processes which however are nearly the same for the three cases. As a result, the hydrographs of the later discharge peaks have minor differences for different floodplain width.

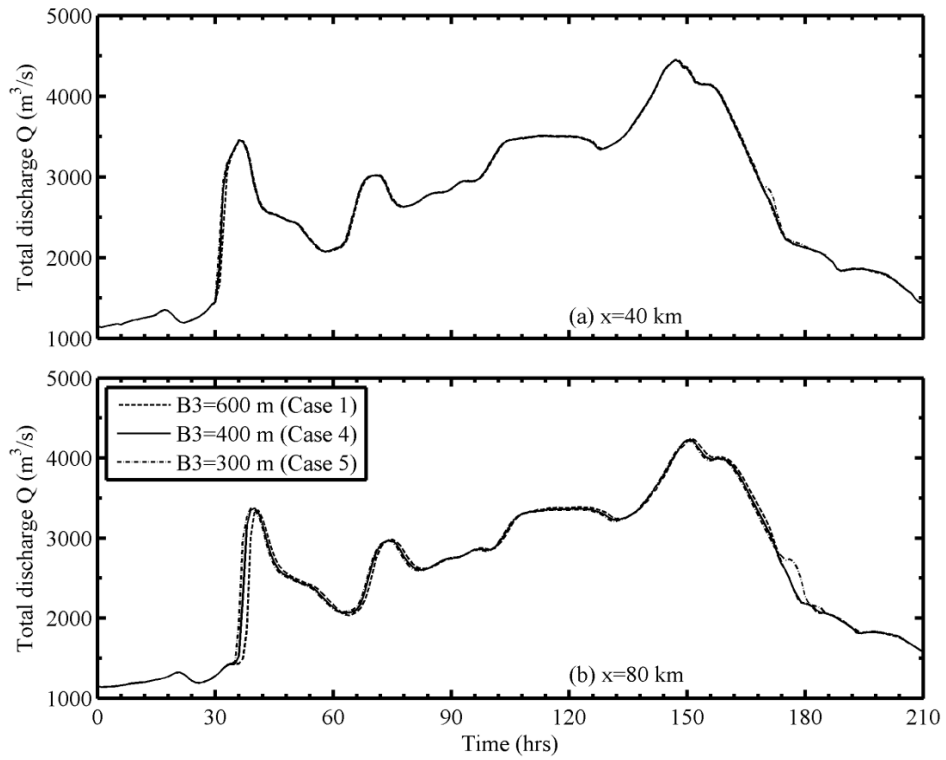


Figure 8 Computed discharge hydrographs for different floodplain width at (a) $x=40$ km, (b) $x=80$ km.

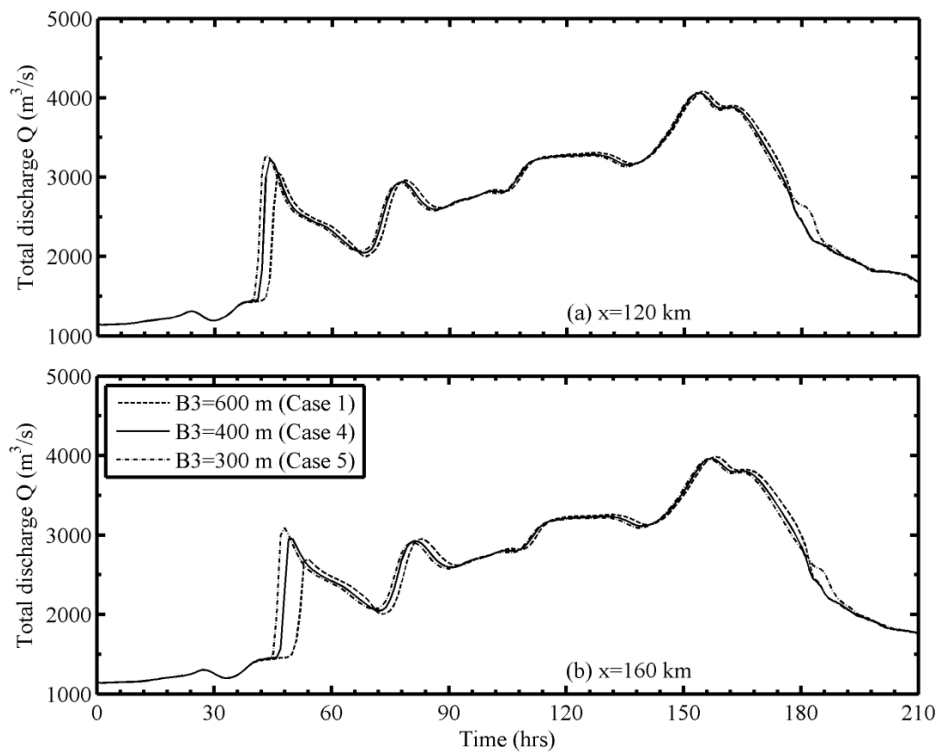


Figure 9 Computed discharge hydrographs for different floodplain width at (a) $x=120$ km, (b) $x=160$ km.

5.4 Influences of bed roughness variation

Previously we did a detailed investigation on the effects of bed roughness variation for two HF events in the Yellow River reach with a simple rectangular cross-sectional profile (Li et al., 2014). The findings showed that the change of bed roughness could play an important role in the downstream peak discharge increase. Here we therefore test the effects of roughness variation in a channel-floodplain reach by comparing Case 2 and Case 8, though observed data of the roughness variation cannot be found for this flood.

The results show that the behavior of the second flood peak becomes qualitatively different when a varying bed roughness is considered. A downstream increasing peak discharge is computed for this flood peak in Case 8 (Fig. 10) when the Manning roughness decreases by about 27% (from 0.011 to 0.008) using Eq. (15). In comparison, a considerable decrease of the second flood peak is computed in the downstream reach of Case 2 by a constant bed roughness (Fig. 6b). Moreover, the variation of bed roughness also contributes to strong floodplain deposition in Case 8. Comparing with Case 2 for which no deposition occurs during the second flood, Case 8 shows a relatively large deposition near the transitional point of the channel and floodplain in this period (Fig. 11). Therefore, a deeper channel for Case 8 is developed through floodplain deposition when the process of channel erosion nearly remains the same in the two cases (comparing Figs. 4b and 11). Such morphological change could accommodate more channel flow, and might in turn affect the flood propagation contributing to the downstream discharge increase. However, neither the roughness decrease nor the associated morphological change is sufficient to introduce an increasing peak discharge as large as what is observed in the field.

The other flood peaks in both Cases 2 and 8 have a decreasing trend in the downstream direction (Figs. 6b and 10). It implies that the variation of bed roughness cannot explain the peak discharge increase for the 1992 HF passing the channel-floodplain reach.

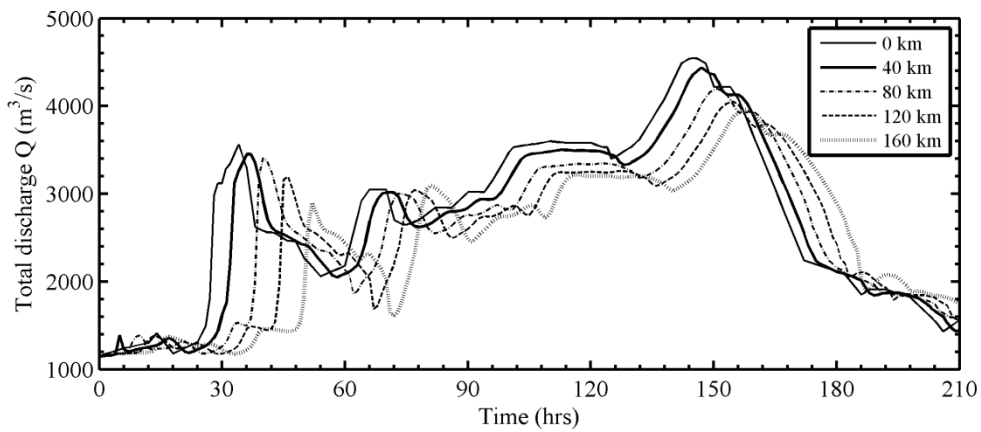


Figure 10 Computed discharge evolution for Case 8 with a varying bed roughness.

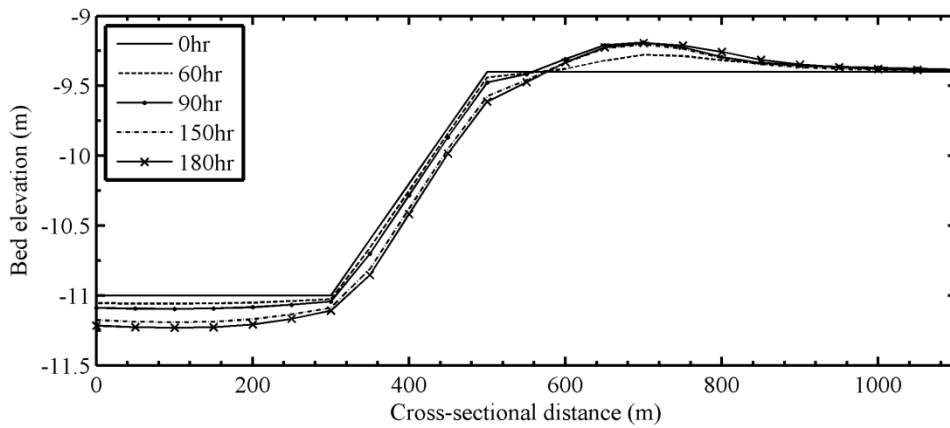


Figure 11 Cross-sectional changes at $x=40$ km for Case 8 with a varying bed roughness.

6 Results of the 1992 HF in the symmetric channel-floodplain

The cross-sectional area of the symmetric channel-floodplain reach is designed to be the same as that of the asymmetric reach when a certain water level is set. Thus, the comparison between the symmetric and asymmetric types can show how the shape of the cross-section affects flood propagation and morphology. Here, we consider two cases with a small and a moderate erosion rate, respectively. For Case 6 of a small erosion rate ($M=1.0 \times 10^{-4}$), both the channel and floodplain are continuously eroded when the HF passes by (Fig. 12a). Due to narrower floodplain of the symmetric type, more erosion occurs at the edge of the channel and floodplain. In comparison,

floodplain deposition occurs in the waning stage of the fourth flood peak for the asymmetric type of Case 2 (Fig. 4b). The erosion processes of the main channel are quite similar for the two types possibly due to the minor effects of relatively small floodplain deformation. For Case 7 of a moderate erosion rate ($M=2.5 \times 10^{-4}$), stronger erosion develops in the main channel and the edge of the channel-floodplain (Fig. 12b) though the sediment bed should be more difficultly eroded by a larger critical bed shear stress when comparing with Case 2. This provides the sediment source for deposition near the sidewalls of the floodplain.

Due to more floodplain erosion, larger flow discharge is computed in the symmetric reach than the asymmetric reach (Comparing Cases 6 and 2), especially during the third and fourth flood peaks (Fig. 13). However, the magnitude of the morphological change in the symmetric reach is still insufficient to trigger a peak discharge increase.

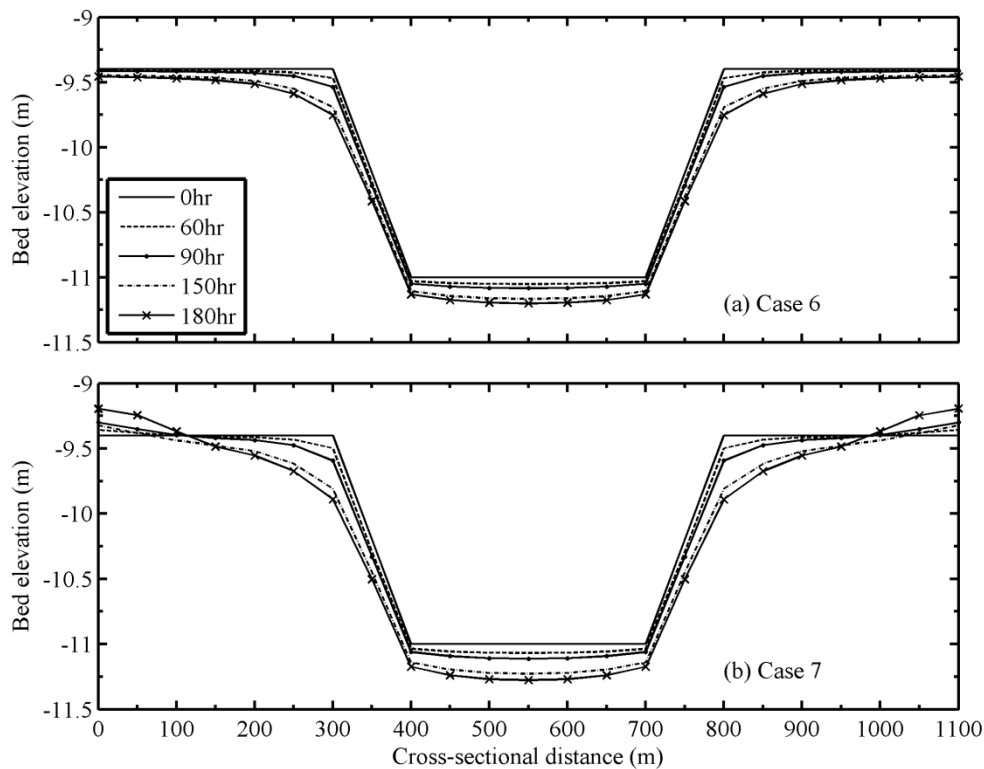


Figure 12 Cross-sectional changes at $x=40$ km for (a) Case 6 with $M=1.0 \times 10^{-4}$, (b) Case 7 with $M=2.5 \times 10^{-4}$.

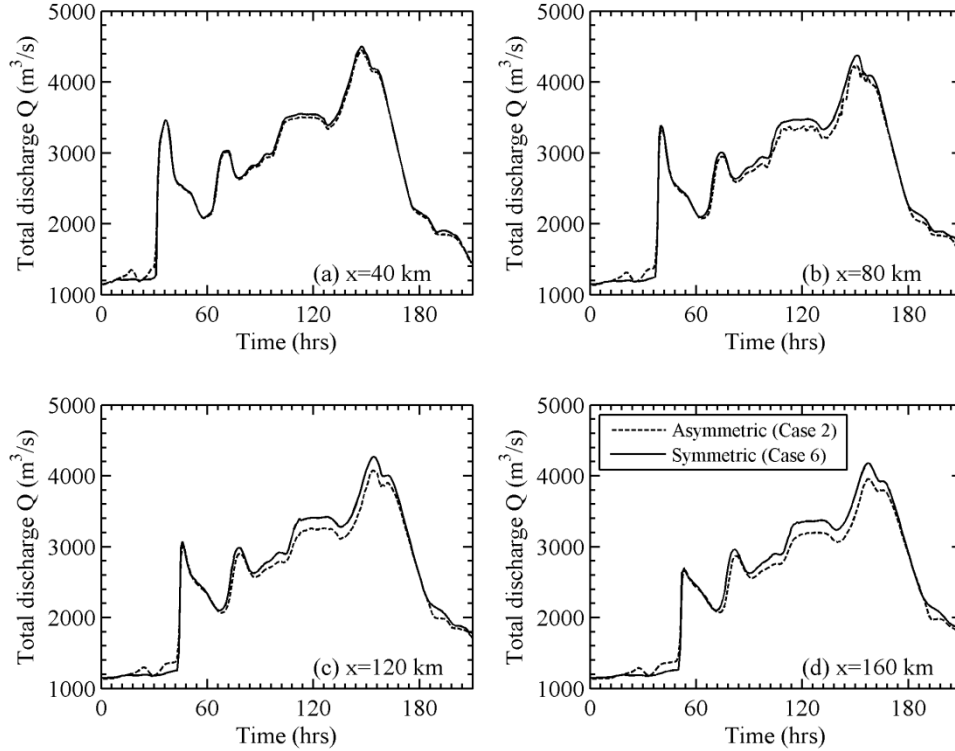


Figure 13 Comparison of discharge hydrograph at distinct locations for Cases 2 and 6.

7 Discussions

7.1 Geometric assumptions

Due to lack of topographic data, we focus on the mechanism study and run the numerical modeling with assumptions for the initial channel-floodplain geometry. At a cross-section, a simple shape is assumed consisting of a trapezoidal channel and flat floodplains (see Fig. 3). Along the channel-floodplain reach, the cross-section is assumed unchanged leading to a longitudinally uniform river course. This simplification may avoid uncertainties raising from geometric complexity and can facilitate a clear understanding of how the floodplain and main channel interact each other during a HF. However, we are also aware of the importance of incorporating the geometric features that is more close to nature, e.g., a complex channel with secondary floodplains or discontinuous floodplains along the water course. Such conditions will complicate not only the fluvial processes but also the flow exchange of channel-floodplain. Moreover, human interventions to the river system are always existed, such as housing/farming on the floodplain and engineering works along channel banks. These will absolutely affect the geometric structure and thus the flow

pattern and morphological change. But currently it is rather difficult to take a full consideration of these effects in such a large spatial scale due to the lack of detailed information.

7.2 Flood hydrographs in response to morphological change

The present numerical results show that the magnitude of floodplain deformation (mainly deposition) is far smaller than that of channel deformation (mainly erosion) during a HF. This is in accordance with the observed morphological change after some HF events in the lower Yellow River, i.e., 1959 HF (van Maren et al., 2009b), 1973 and 1977 HF (Qi et al., 2010). It indicates that the change of the main channel profile should play a dominant role in flood propagation while the morphological effects of floodplain deformation are rather limited. This is true for conditions of relatively weak and moderate erosion/deposition settings (e.g., Cases 1 and 2). In such cases, the hydrographs of the flood exhibit similar trend along the river course when only the magnitude decreases with distance due to energy loss. However, the role of floodplain deformation could be large in the case of relatively strong erosion/deposition settings (e.g., Case 3). The shallow overtopping flow can be blocked or largely decelerated by strong deposition on the floodplain (even though its magnitude is still far smaller than channel erosion), and thus it may contribute to a considerable change of hydrographs at downstream. On the one hand, the downstream discharge peak may have a sharp drop as predicted in Case 3. On the other hand, the discharge peak may be possibly enlarged at downstream (as observed in some HF events in the lower Yellow River), which largely depends on whether and how the blocked/decelerated water volume can return to the main channel.

Based on the numerical results, it seems difficult to predict a downstream peak discharge increase for a longitudinally uniform channel-floodplain reach of a large spatial scale. The large floodplain width results in shallow overtopping flow and low floodplain deposits reducing its role on channel deepening. Therefore, the flow acceleration due to channel deepening is insufficient for later parts of the flood to catch up with the former flood peak. Moreover, the insufficient channel deepening cannot form a large transverse slope of the water surface for more water flowing back to channel. To further confirm this understanding, additional numerical cases are presented to see the effects of longitudinally varying channel-floodplain reach.

7.3 Effects of longitudinally varying channel-floodplain reach

Here we run two more simulations for the 1992 HF in two longitudinally varying channel-floodplain reaches (Figs. 14-15). The motivation of the two channel-floodplain topographies are the discontinuous floodplains divided by intermittent water storage area (Profile A) and houses/farming banks (Profile B). The spatial scales of the two reaches are the same as that of the former longitudinally uniform reach, with a total length of 160 km and a total width of 1100 m. Here, we define $L_1=20$ km, $L_2=30$ km, $L_3=25$ km, $B_1=300$ m, $B_2=200$ m, $B_3=600$ m, $B_4=300$ m. The channel depth and bed slope are the same as that in the uniform reach (see section 4.2). Other model settings follow Case 1.

The numerical results show that both in Profile A and B the peak discharge of the HF decreases along the river course (Fig. 16). While the downstream peak discharge decreases uniformly in Profile B, a sharp decrease is observed from $x=60$ km to $x=80$ km in Profile A. This decrease is probably due to the detention effects of the water storage area by channel widening. The time evolution of bed profiles at some representative cross-sections is shown in Figs. 17-18. In Profile A, the channel widening leads to less channel erosion and no more floodplain deposition (Figs. 17 (b), (d)) while sediment still deposits on the floodplain with no widening channel (Figs. 17 (a), (c)). In Profile B, the highland (B_4 in Fig. 15) at the interface of the channel and floodplain prevents sediment from depositing on the floodplain (Figs. 18 (b), (d)) while deposition still occurs on the normal floodplain without structure disturbances (Figs. 18 (a), (c)). This further confirms the above understanding derived from Figs. 4 and 6.

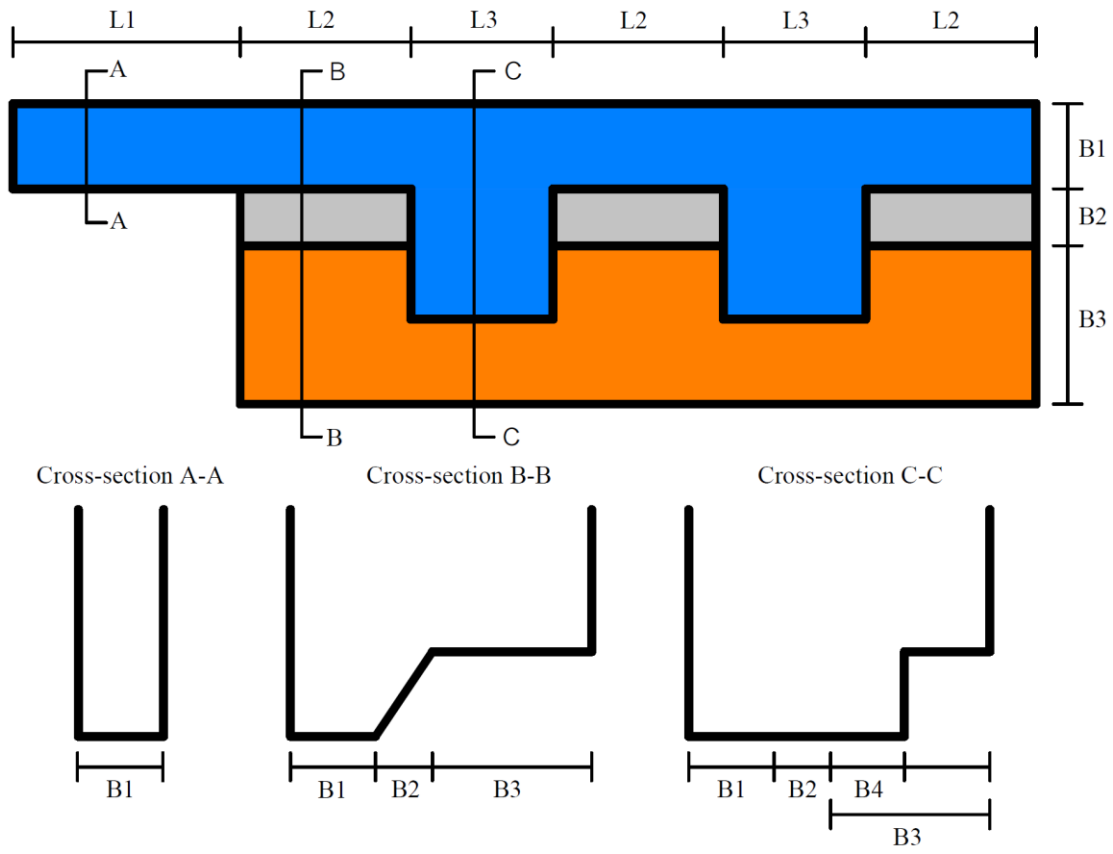


Figure 14 Sketch of the longitudinally varying channel-floodplain reach (Profile A).

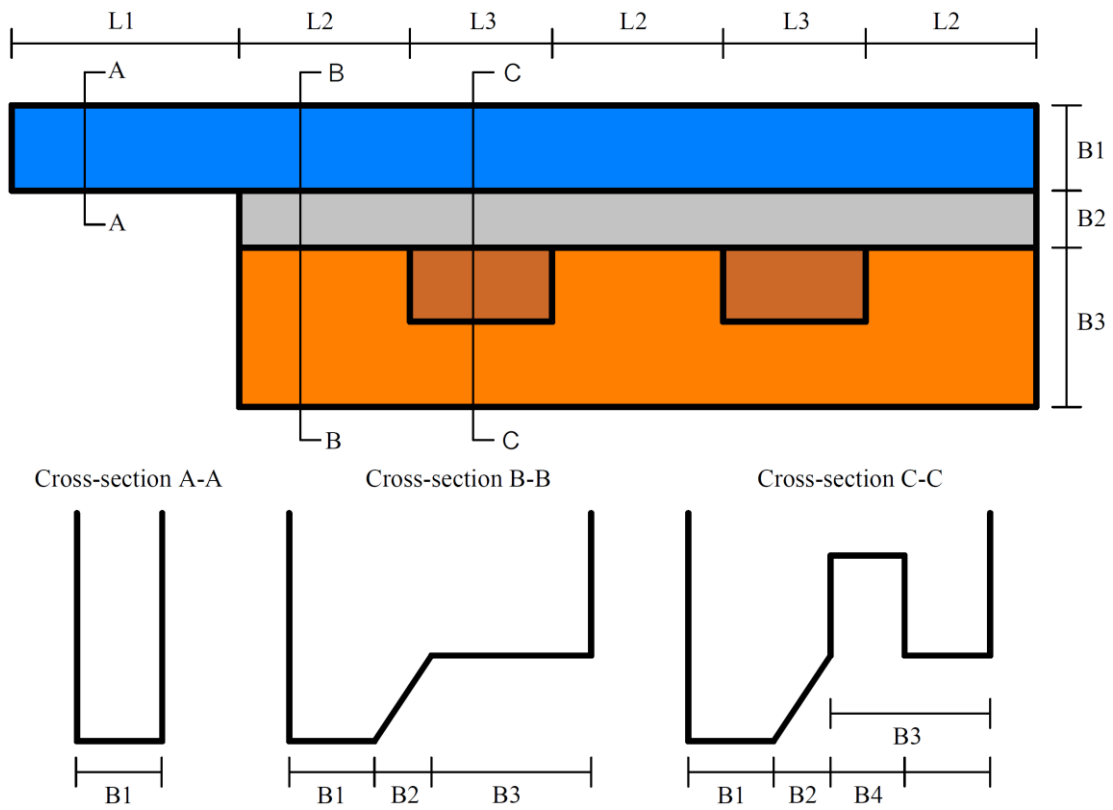


Figure 15 Sketch of the longitudinally varying channel-floodplain reach (Profile B).

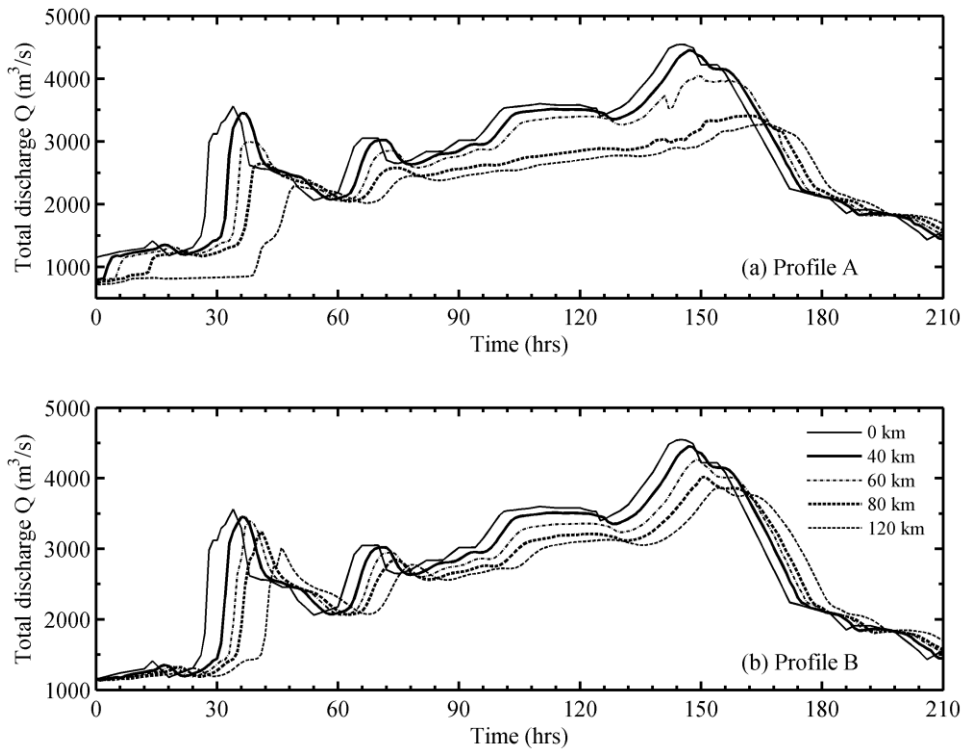


Figure 16 Discharge evolution for (a) Profile A and (b) Profile B.

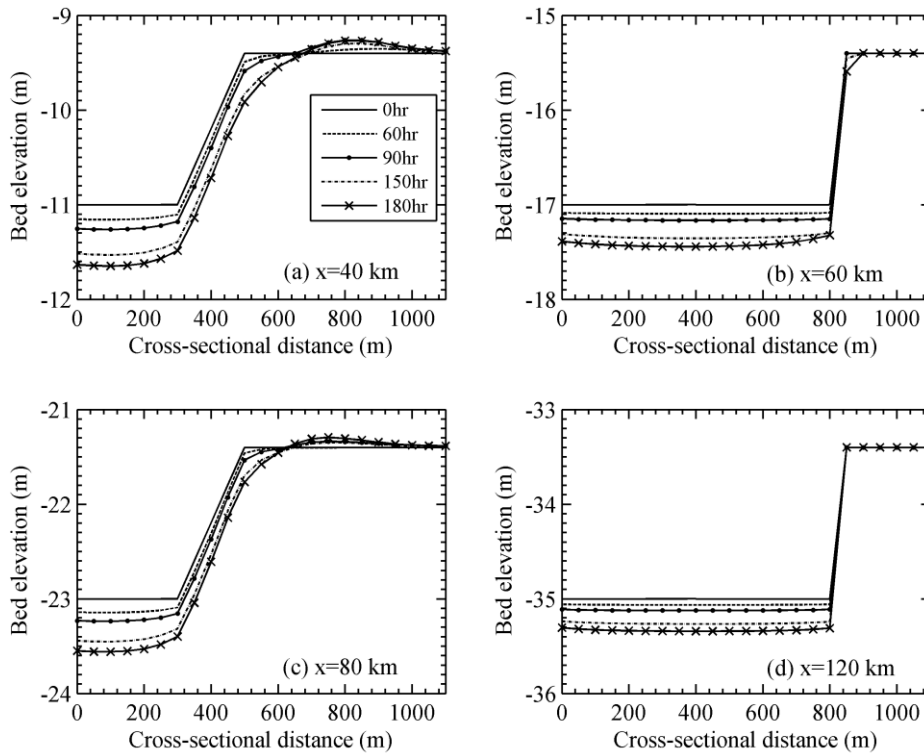


Figure 17 Time evolution of bed profiles at representative cross-sections of Profile A.

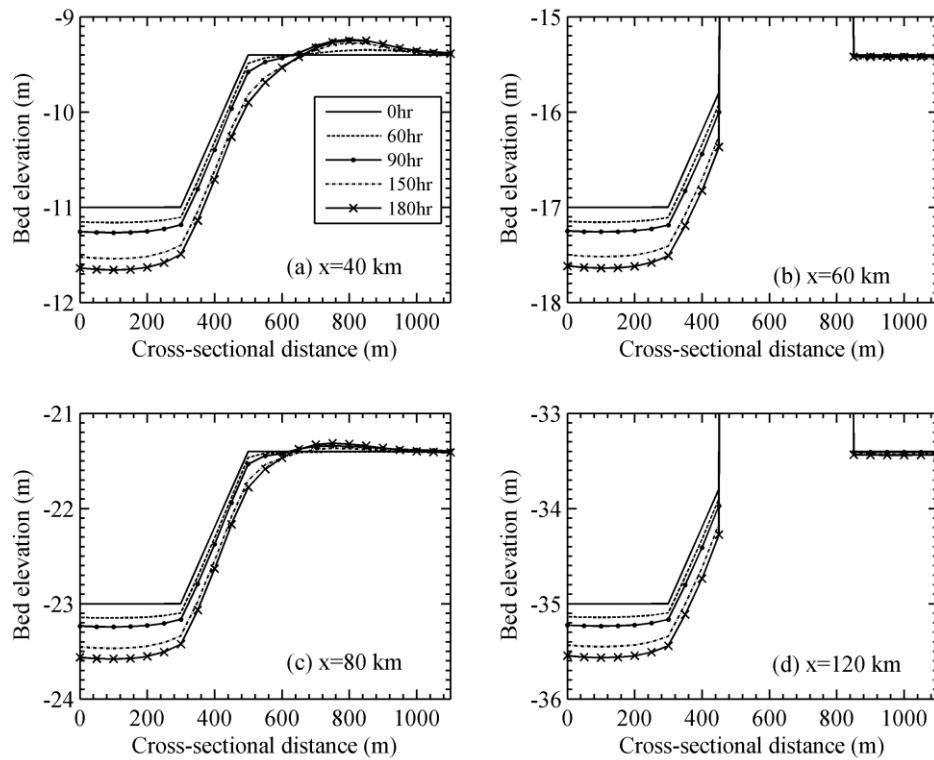


Figure 18 Time evolution of bed profiles at representative cross-sections of Profile B.

7.4 Effects of different turbulence closure models

Many depth-averaged turbulence closure models for shallow clear water/low sediment-laden flows can be found in the literature, such as parabolic eddy viscosity model (Cea et al., 2007; Duan, 2004; Wu et al., 2004; Xia et al., 2012), mixing length model (Jia and Wang, 1999; Cea et al., 2007), $k - \epsilon$ model (Rastogi and Rodi, 1978; Babarutsi and Chu, 1991), and algebraic stress model (Cea et al., 2007), etc. However, to our knowledge there have been no turbulence closure models specific for the case of hyperconcentrated floods, and therefore the above turbulent closures are used (e.g., Wu et al., 2004; Xia et al., 2012).

We have made a comparison of the mixing length model and the parabolic eddy viscosity model for Cases 1-5 of the asymmetric reach. The findings show that in most conditions of minor/moderate erosion the two models result in nearly identical

channel-floodplain patterns (e.g., $t=60, 90$ hr of Case 1 and 3 in Figs. 19-20). Slight differences are observed in some conditions of relatively strong erosion, of which however the effects on the overall channel-floodplain pattern are negligible (e.g., $t=150, 180$ hr of Case 1 and 3 in Figs. 19-20). Considering the duration of a HF in the Yellow River is typically about 200 hr, such slight differences cannot accumulate to a larger extent as compared with those shown below. These are attributed to the following fact, that is, the flooding process is dominated by convection (both along the main stream direction and in the cross-sectional direction), whereas lateral mass and momentum exchange due to turbulent diffusions (e.g., van Prooijen, 2005) are essentially secondary.

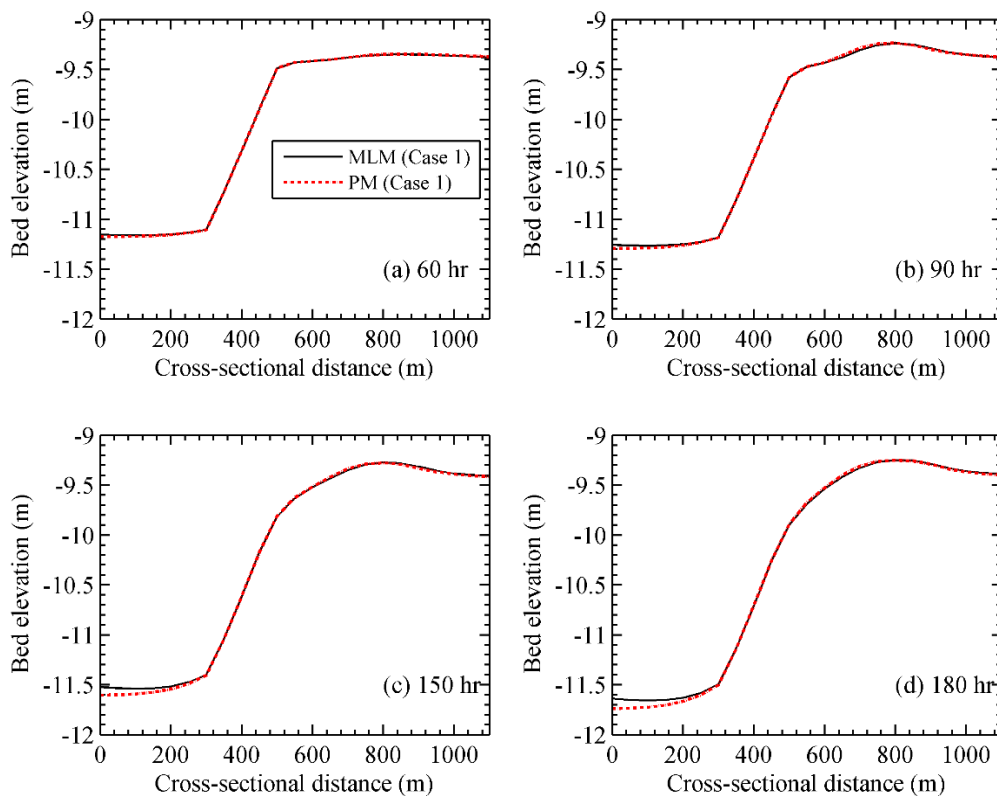


Figure 19 Detailed comparison of bed profile at distinct instants for the mixing length model (MLM) and the parabolic eddy viscosity model (PM) in Case 1 at $x=40$ km.

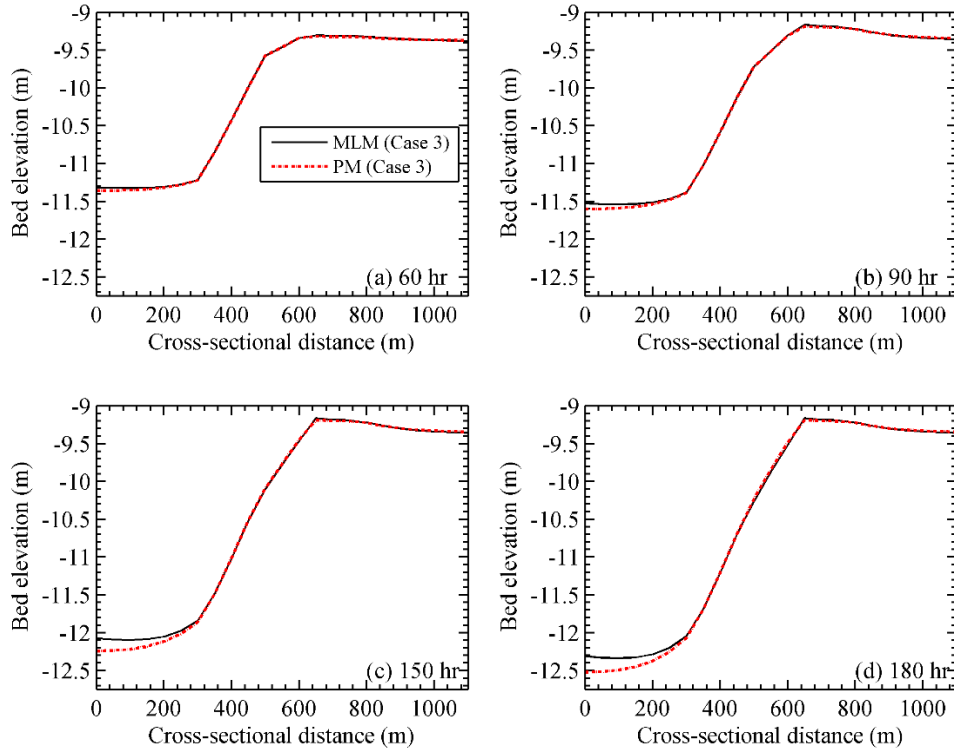


Figure 20 Detailed comparison of bed profile at distinct instants for the mixing length model (MLM) and the parabolic eddy viscosity model (PM) in Case 3 at $x=40$ km.

8 Conclusions

The mechanisms of the HF propagating in a dynamic channel-floodplain system have been numerically investigated by a 2-D depth-averaged model of non-capacity sediment transport. The interactions between water flow, sediment transport, and morphological changes have been fully considered in the modelling through a set of fully coupled governing equations and a synchronous solution method. The major findings can give some indications to answer the four questions raised in the end of the introduction part:

- (1) With a suitable erosion rate (M), the typical morphological features of channel erosion and floodplain deposition during a HF can be successfully reproduced by the present model. Due to channel-floodplain interactions, a decrease of the erosion rate does not simply yield less channel erosion and more floodplain deposition, but may cause both channel and floodplain erosion. Similarly, an increase of the erosion rate does not lead to more channel-floodplain erosion, but may strengthen channel erosion and floodplain deposition. The floodplain width plays a significant role in shaping floodplain deposition but marginally affect

channel erosion patterns probably because that the floodplain deformation is far smaller than that of the channel.

- (2) The behavior of channel erosion and floodplain deposition can play an important role in the downstream HF propagation. For relatively weak and moderate erosion/deposition settings, the overtopping flow is sufficiently deep to transport large portion of suspended sediment without the occurrence of dry areas on the floodplain. The peak discharge is observed to decrease uniformly in the downstream direction due to energy loss. For relatively strong erosion/deposition settings, the strong channel deepening may weaken the flood overtopping and thus very shallow flow may occur on the floodplain. Meanwhile, the floodplain deposition can be strengthened by strong channel erosion possibly resulting in flow blockage or deceleration on the floodplain. Therefore, a sharp drop of the flood peak is predicted in the downstream.
- (3) A downstream constant or slightly increase of the flood peak has been predicted in our work. One reason might be flow acceleration by bed roughness reduction, for which the mechanism has been thoroughly studied in our previous work (Li et al., 2014). The other might be related to strong channel erosion, which leads to either channel flow acceleration or the returning of the overtopping flow to the channel. However, the downstream increase of the flood peak is not obvious in the current study, the underlying mechanisms of its occurrence in channel-floodplain reach deserve further research.
- (4) In the case of overtopping, the symmetric type of the channel-floodplain reach is more likely to be eroded than the asymmetric type mainly around the edge of the channel-floodplain area. Therefore, a larger flow discharge is observed in the symmetric type than that in the asymmetric type. In the case of longitudinally discontinuous channel-floodplain divided by either water storage areas or housing/farming banks, floodplain deposition diminishes at the discontinuous locations. This discontinuity in geomorphology leads to a downstream decreasing peak discharge.

Appendix

Two model tests are presented here. The first test is the preservation of static water at a 1-D surface-piercing hump, by which the C-property of the model with dry-wet

interface has been tested. It is important because that in reality, the overflowing could be static in some parts of the floodplain of complex topography. The second test is 2-D dam-break flow over an initially dry erodible bed, by which the model ability to well capture the moving dry/wet front in highly unsteady flow and to accurately predict the morphological evolution has been tested. This is also of crucial importance as hyperconcentrated flow are often characterized by highly unsteady flow and rapid/strong morphological changes. And the floodplain overflowing could encounter the moving dry/wet problem.

A1 Preservation of static water at a 1-D surface-piercing hump

A test conducted in a schematized one-dimensional configuration with dry-wet interface (Bermúdez and Vázquez-Cendón, 1994; Castro-Dáz et al., 2005) has been done to examine the well-balanced property of the present model. It consists of a surface-piercing hump at the center of a 1 m long domain with the bed elevation defined by

$$z(x) = \max[0, 0.25 - 5(x - 0.5)^2] \quad (\text{A1})$$

Initially the hump is partially submerged by water at rest. The water level is determined by $\zeta = \max(0.1, z)$. Closed walls are imposed at the boundaries and bed friction is assumed negligible. The computational domain is discretized by $\Delta x = 0.01$ m and the total computational time is 200 s.

For water at rest, the analytical water depth equals to the initial water depth and the analytical discharge should be zero. The numerical results demonstrate that the error norms (i.e., $L_1(h), L_1(q), L_\infty(h), L_\infty(q)$) for water depth and flow discharge are exactly zero during the whole computational time span. Taking two distinct time instants as an example, Figure A1 shows the initially horizontal water surface can be exactly preserved by the SGM version with zero flow discharge. It is also worth noting that the preservation of the C-property by the SGM version does not depend on the grid resolution. Therefore, the SGM version is well-balanced and should be applicable to field scales of irregular topography especially for the static water conditions.

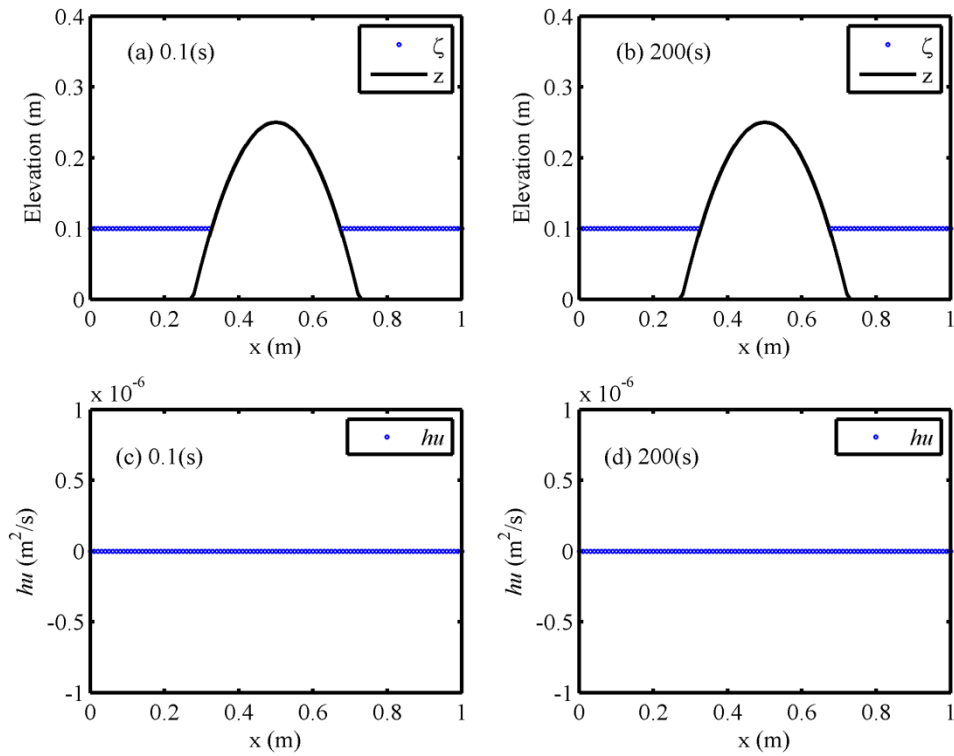


Figure A1 Computed water depth and discharge at distinct instants.

A2 2-D mobile bed dam-break flow

The applicability of the SGM version to conditions of highly unsteady flow and rapid morphological changes has been tested by a 2-D mobile bed dam-break experiment conducted at the Civil Engineering Laboratory of the Universite Catholique de Louvain, Belgium (Zech et al., 2008). This case was previously simulated by our original model of DGM version (Li et al., 2013). In the present test, the tolerance depths for dry-wet treatment are 0.0004 and 0.0005 m. Other parameters and empirical relations are the same as those used in Li et al. (2013).

The computed results of water level histories and final bed elevation by the SGM version are compared with the experimental data at corresponding locations (see Fig. A2) in Figures A3 and A4 respectively. It shows that the SGM version predicts satisfactorily the water level and bed elevation for this test.

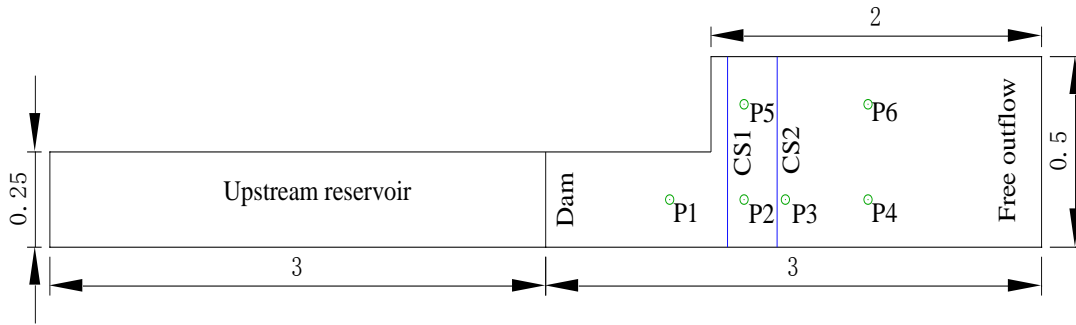


Figure A2 Sketch of the experiment flume (unit: m).

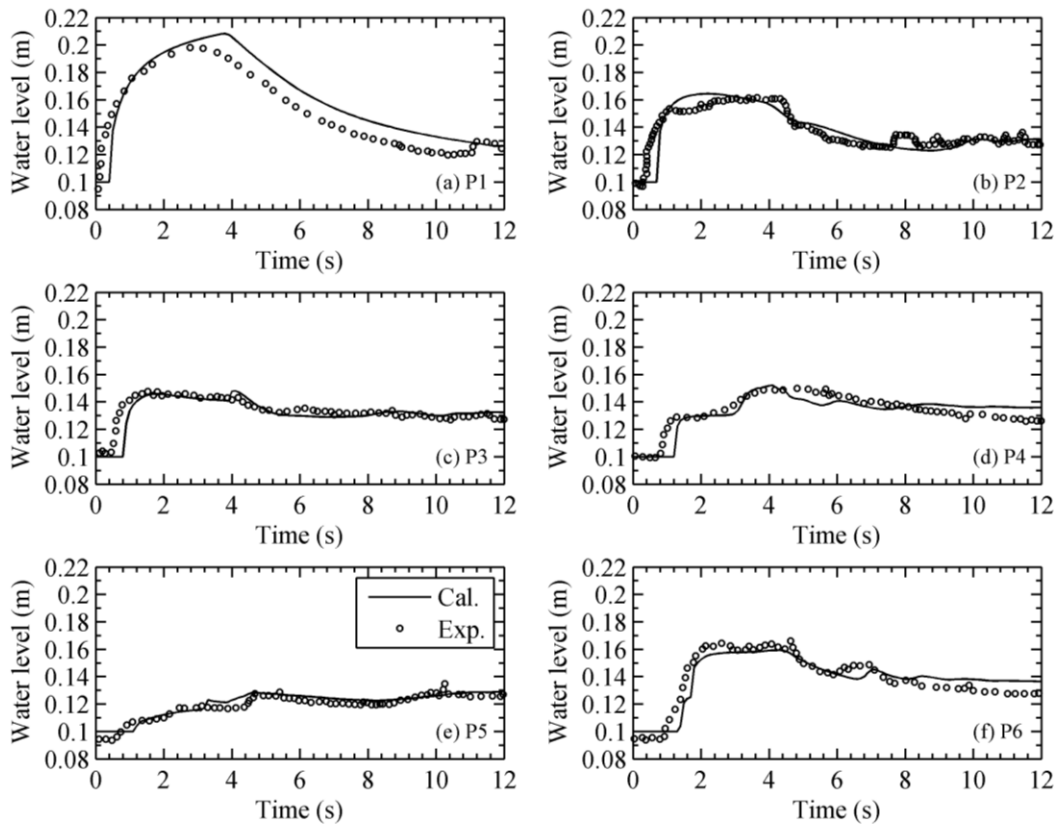


Figure A3 Comparison of the calculated water level and experiment data at distinct gauges.

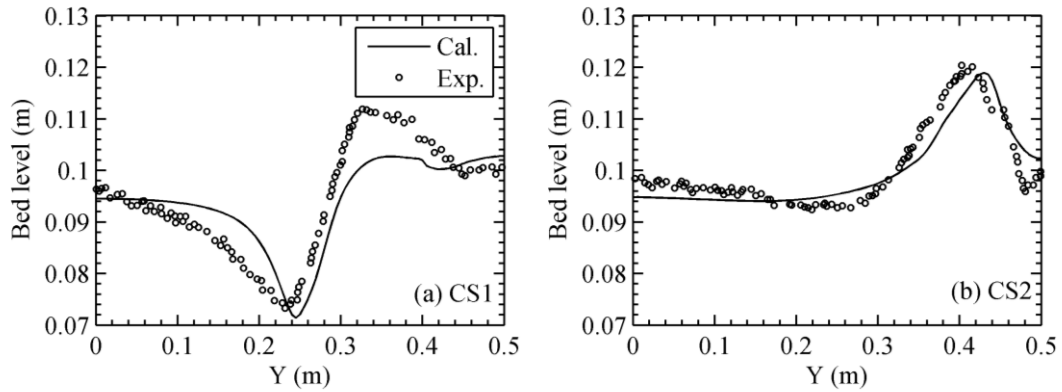


Figure A4 Comparison of calculated final bed elevation and experiment data at (a) CS1 and (b) CS2.

Acknowledgements

The study is supported by the National Science Foundation of China (No. 11502233) and Science Foundation of Zhejiang Province (No. LQ15E090002).

References

- Babarutsi, S., and V. H. Chu (1991), A two-length-scale model for quasi-two-dimensional turbulent shear flows, In: Proceedings of 24th IAHR congress, Madrid, Spain, volume C, 51-60.
- Batalla, R. J., C. De Jong, P. Ergenzinger, and M. Sala (1999), Field observations on hyperconcentrated flows in mountain torrents, *Earth Surface Processes and Landforms*, 24, 247-253.
- Bermúdez, A., and M. E. Vázquez-Cendón (1994), Upwind methods for hyperbolic conservation laws with source terms, *Computers and Fluids*, 23(8):1049-1071.
- Breien, H., F. V. De Blasio, A. Elverhøy, and K. Høeg (2008), Erosion and morphology of a debris flow caused by a glacial lake outburst flood, western Norway, *Landslides*, 5, 271-280.
- Cao, Z. X., G. Pender, and P. Carling (2006), Shallow water hydrodynamic models for hyperconcentrated sediment-laden floods over erodible bed, *Advances in Water Resources*, 29, 546-557.

- Cao, Z. X., Z. J. Li, G. Pender, and P. Hu (2012), Non-capacity or capacity model for fluvial sediment transport, *Water Management*, 165(WM4), 193-211.
- Capra, L. (2007), Volcanic natural dams: identification, stability and secondary effects, *Natural Hazards*, 43, 45-61.
- Castro-Dáz, M. J., A. M. Ferreiro, J. A. García-Rodríguez, J. M. González-Vida, J. Macías, C. Parés, and M. E. Vázquez-Cendón (2005), The numerical treatment of wet/dry fronts in shallow flows: application to one-layer and two-layer systems, *Mathematical and Computer Modelling*, 42:419-439.
- Cea, L., J. Puertas, and M. Vázquez-Cendón (2007), Depth averaged modelling of turbulent shallow water flow with wet-dry fronts, *Archives of Computational Methods in Engineering*, 14, 303-341.
- Chien, N. (ed.) (1989), *A study of Hyperconcentrated flows*, Tsinghua University Press, Beijing (in Chinese).
- Chien, N., and Z. H. Wan (1983), *Mechanics of Sediment Transport*, Science Press, Beijing, China (in Chinese).
- Cohen, H., and J. B. Laronne (2005), High rates of sediment transport by flashfloods in the Southern Judean Desert, Israel, *Hydrological Processes*, 19, 1687-1702.
- Cronin, S. J., J. A. LeCointre, A. S. Palmer, and V. E. Neall (2000), Transformation, internal stratification, and depositional processes within a channelized, multi-peaked lahar flow, *New Zealand Journal of Geology and Geophysics*, 43, 117-128.
- Duan, J. G. (2004), Simulation of flow and mass dispersion in meandering channels, *Journal of Hydraulic Engineering*, 130(10), 964-976.
- Harten, A., B. Engquist, S. Osher, and S. Chakravarthy (1987), Uniformly high order accuracy essentially non-oscillatory schemes III, *Journal of Computational Physics*, 71, 231-303.
- Hu, P., Z. Cao, G. Pender, and G. M. Tan (2012), Numerical modelling of turbidity currents in Xiaolangdi Reservoir, Yellow River, China, *Journal of Hydrology, Elsevier*, 464-465, 41-53.
- Jia, Y. F., and S. S. Y. Wang (1999), Numerical model for channel flow and morphological change studies, *Journal of Hydraulic Engineering*, 125(9), 924-933.

- Jiang, E. H., L. J. Zhao, and Z. L. Wei (2006), Mechanism of flood peak increase along the Lower Yellow River and its verification, *Shuili Xuebao*, 37(12), 1454-1459 (in Chinese).
- Kostaschuk, R., T. James, and R. Rishi (2003), Suspended sediment transport during tropical cyclone floods in Fiji, *Hydrological Processes*, 17, 1149-1164.
- Laronne, J. B., and I. Reid (1993), Very high rates of bed load sediment transport by ephemeral desert rivers, *Nature*, 366, 148-150.
- Li, G. Y. (2008), Analysis on mechanism of peak discharge increasing during flood routing in lower reaches of Yellow River, *Shuili Xuebao*, 39(5), 511-517 (in Chinese).
- Li, W., H. J. de Vriend, Z. Wang, and D. S. van Maren (2013), Morphological modeling using a fully coupled, total variation diminishing upwind-biased centered scheme, *Water Resources Research*, 49, 3547-3565, doi: 10.1029/wrcr.20138.
- Li, W., Z. B. Wang, D. S. van Maren, H. J. de Vriend, and B. S. Wu (2014), Peak discharge increase in hyperconcentrated floods, *Advances in Water Resources*, 67, 65-77.
- Lirer, L., A. Vinci, I. Alberico, T. Gifuni, F. Bellucci, P. Petrosino, and R. Tinterri (2001), Occurrence of inter-eruption debris flow and hyperconcentrated flood-flow deposits on Vesuvio volcano, Italy, *Sedimentary Geology*, 139, 151-167.
- Long, Y. Q., and Y. F. Zhang (2002), Study on the Yellow River sediment from the viewpoint of total sediment, *Yellow River*, 24(8), 28-29 (in Chinese).
- Maizels, J. (1989), Sedimentology, paleoflow dynamics and flood history of jökulhlaup deposits: paleohydrology of Holocene sediment sequences in southern Iceland sandur deposits, *Journal of Sedimentary Petrology*, 59, 204-223.
- Manville, V., J. D. L. White, B. F. Houghton, and C. J. N. Wilson (1999), Palaeohydrology and sedimentology of a post-1.8 ka breakout flood from intracaldera Lake Taupo, North Island, New Zealand, *Geological Society of America Bulletin*, 111, 1435-1447.
- Van Maren, D. S., J. C. Winterwerp, Z. Y. Wang, and P. Qi (2009a), Suspended sediment dynamics and morphodynamics in the Yellow River, China, *Sedimentology*, 56(3), 785-806, doi: 10.1111/j.1365-3091.2008.00977.x.

- Van Maren, D. S., J. C. Winterwerp, B. S. Wu, and J. J. Zhou (2009b), Modelling hyperconcentrated flow in the Yellow River, *Earth Surface Processes and Landforms*, 34(4), 596-612, doi: 10.1002/esp.1760.
- Partheniades, E. (1965), Erosion and deposition of cohesive soils, *Journal of the Hydraulic Division, ASCE* 91(HY1), 105-139.
- Pierson, T. C. and J. E. Costa (1987), A rheologic classification of sub-aerial sediment-water flows, In: Costa, J. E., and G. F. Wieczorek (Eds.), *Debris Flows/Avalanches: Process, Recognition, and Mitigation, Reviews in Engineering Geology*, 7, Geological Society of America, 1 – 12.
- Pierson, T. C., and K. M. Scott (1985), Downstream dilution of a lahar: transition from debris flow to hyperconcentrated streamflow, *Water Resources Research*, 21, 1511-1524.
- van Prooijen, B. C., J. A. Battjes, and W. S. Uijtewaal (2005), Momentum exchange in straight uniform compound channel flow, *Journal of hydraulic engineering*, 131(3), 175-183.
- Qi, P., and W. X. Li (1996), Evolutional characteristics of hyperconcentrated flow in braided channel of the Lower Yellow River, *International Journal of Sediment Research*, 11(3), 49-57.
- Qi, P., Z. Y. Sun, and H. H. Qi (2010), *Flood discharge and sediment transport potentials of the Lower Yellow River and development of an efficient flood discharge channel*, Yellow River Hydraulics Press, Zhengzhou, China (in Chinese).
- Rastogi, A. K., and W. Rodi (1978), Predictions of heat and mass transfer in open channels, *Journal of Hydraulics Division*, 104(3), 397–420.
- Richardson, J. F., and W. N. Zaki (1954), Sedimentation and fluidization, Part I. *Transactions of the Institution of Chemical Engineers*, 32, 35-53.
- Russell, H. A. J., and R. W. C. Arnott (2003), Hydraulic-jump and hyperconcentrated-flow deposits of a glacial subaqueous fan: Oak Ridges Moraine, Southern Ontario, Canada, *Journal of Sedimentary Research*, 73(6), 887-905.

- Siviglia, A., G. Stecca, D. Vanzo, G. Zolezzi, E. F. Toro, and M. Tubino (2013), Numerical modelling of two-dimensional morphodynamics with applications to river bars and bifurcations, *Advances in Water Resources*, 52, 243-260.
- Smith, G. A. (1986), Coarse-grained non-marine volcanoclastic sediment: terminology and depositional process, *Geological Society of America Bulletin*, 97, 1-10.
- Smith, G. A. (1987), The influence of explosive volcanism on fluvial sedimentation: the Deschutes Formation (neogene) in central Oregon, *Journal of Sedimentary Petrology*, 57(4), 613-629.
- Sohn, Y. K., M. Y. Choe, and H. R. Jo (2002), Transition from debris flow to hyperconcentrated flow in a submarine channel (the Cretaceous Cerro Toro Formation, southern Chile), *Terra Nova*, 14(5), 405-415.
- Sohn, Y.K., C. W. Rhee, and B. C. Kim (1999), Debris flow and hyperconcentrated flood-flow deposits in an alluvial fan, northwestern part of the Cretaceous Yongdong Basin, Central Korea, *Journal of Geology*, 107, 111-132.
- Stecca, G., A. Siviglia, and E. F. Toro (2010), Upwind-biased FORCE schemes with applications to free-surface shallow flows, *Journal of Computational Physics*, 229, 6362-6380.
- Stecca, G., A. Siviglia, and E. F. Toro (2012), A finite volume upwind-biased centred scheme for hyperbolic systems of conservation laws. Applications to shallow water equations, *Communications in Computational Physics*, 12(4), 1183 - 214.
- Svendsen, J., H. Stollhofen, C. B. E. Krapf, and I. G. Stanistreet (2003), Mass and hyperconcentrated flow deposits record dune damming and catastrophic breakthrough of ephemeral rivers, Skeleton Coast Erg, Namibia, *Sedimentary Geology*, 160, 7-31.
- Thouret, J. C. (1999), Volcanic geomorphology-an overview, *Earth-Science Reviews*, 47, 95-131.
- Toro, E. F. (2001), *Shock-capturing methods for free-surface shallow flows*, Wiley and Sons Ltd., England.
- Toro, E. F. (2009), *Riemann solvers and numerical methods for fluid dynamics: a practical introduction (3rd edition)*, Springer-Verlag Press, Berlin.
- Wan, Z. H., and Z. Y. Wang (1994), Hyperconcentrated flow, IAHR monograph series, Balkema, Rotterdam, The Netherlands.

- Wang, Z. Y., P. Qi, and C. S. Melching (2009), Fluvial hydraulics of hyperconcentrated Floods in Chinese rivers, *Earth Surface Processes and Landforms*, 34, 981-993.
- Wang, G. Q., J. Q. Xia, and H. W. Zhang (2002), Theory and practice of hyperconcentrated sediment-laden flow in China, paper presented at Proceedings of the 13th Congress of the Asia and Pacific Division, IAHR, Singapore, 1055-1071.
- Wilcox, A. C., J. E. O'Connor, and J. J. Major (2014), Rapid reservoir erosion, hyperconcentrated flow, and downstream deposition triggered by breaching of 38m tall Condit Dam, White Salmon River, Washington, *Journal of Geophysical Research: Earth Surface*, 119, 1376-1394.
- Wu, W., E. Jiang, and S. S. Y. Wang (2004), Depth-averaged 2-D calculation of flow and sediment transport in the lower Yellow River, *International Journal of River Basin Management*, 2(1), 51-59.
- Xia, J., Z. Wang, Y. Wang, and X. Yu (2012), Comparison of morphodynamic models for the Lower Yellow River, *Journal of the American Water Resources Association*, 49(1), 114-131.
- Xu, J. X. (1998), A study of physico-geographical factors for formation of hyperconcentrated flows in the Loess Plateau of China, *Geomorphology*, 24, 245-255.
- Xu, J. X. (2004), Effect of human activities on overall trend of sedimentation in the Lower Yellow River, China, *Environmental Management*, 33(5), 637-653.
- Zech, Y., S. Soares-Frazão, B. Spinewine, and N. Le Grelle (2008), Dam-break induced sediment movement: experimental approaches and numerical modelling, *Journal of Hydraulic Research*, 46(2), 176-190.
- Zhang, R. J., and J. H. Xie (1993), *Sedimentation Research in China-Systematic Selections*, China Water Power Press, Beijing.
- Zhao, W. (1996), *Yellow River's Sediment*, Yellow River Water Resources Press, Zhenzhou, China, 595-615 (in Chinese).
- Zhao, L. J., and H. W. Zhang (1997), Study on the characteristics of flow resistance in the Lower Yellow River, *Yellow River*, 19(9), 17-20 (in Chinese).

Zhou, J. G., D. M. Causon, C. G. Mingham, and D. M. Ingram (2001), The surface gradient method for the treatment of source terms in the shallow water equations, *Journal of Computational Physics*, 168(1), 1-25.